Delft University of Technology

Numerical study of hydrodynamic forces and dynamic response for barge type floating platform by computational fluid dynamics and engineering model

Otori, Hiromasa; Kikuchi, Yuka; Rivera-Arreba, Irene; Viré, Axelle

Important note
To cite this publication, please use the final published version (if applicable).
Please check the document version above.

Numerical study of hydrodynamic forces and dynamic response for barge type floating platform by computational fluid dynamics and engineering model

Hiromasa Otori [a], Yuka Kikuchi [a,*], Irene Rivera-Arreba [b], Axelle Viré [c]

[a] *Department of Civil Engineering, School of Engineering, the University of Tokyo, 7-3-1 Hongo, Bunkyo, 113-8656, Tokyo, Japan*
[b] *Department of Marine Technology, Norwegian University of Science and Technology, Høgskoleringen 1, 7034, Trondheim, Norway*
[c] *Wind Energy Section, Delft University of Technology, 2629 HS Delft, the Netherlands*

ABSTRACT

The hydrodynamic coefficients are evaluated by fully nonlinear Navier-Stokes forced oscillation simulations using the volume of fluid method. Richardson extrapolation is employed to obtain the grid-independent solution. The predicted hydrodynamic coefficients are validated by the water tank tests. The applicability of the drag coefficient models as the function of Keulegan-Carpenter numbers in the surge and heave directions are investigated for the barge-type floater by comparing with the numerically predicted drag coefficients. The dynamic response analyses are then conducted using the engineering model with the validated drag coefficient models. The predicted mean values of surge and mooring tension without considering drag forces underestimate the measurements in the high wave height condition, where those with considering drag forces show good agreement, which is analytically explained by the mean drag force being inversely proportional to the square of wave period and proportional to the cube of wave height. Dynamic responses of floater predicted without considering drag forces caused overestimation at the natural frequencies in the heave and pitch directions, while those considering drag forces show good agreement with the measurements.

1. Introduction

Floating offshore wind turbines (FOWTs) are a promising technology for capturing the vast potential offshore wind energy in deep water. Many demonstration projects have been conducted around the world with semi-submersible type and spar type floaters (Hywind Demo, 2009; WindFloat 1, 2009; Fukushima FORWARD,). Barge type floater consisting of simple square panels has been introduced aiming at lowering cost. In 2018, a 2 MW barge-type FOWT was installed in the FLOATGEN project in France (FLOATGEN) and also a 3 MW one in Japan (NEDO Demonstration Project of Next-Generation Offshore Floating Wind Turbine). However, a challenge is that the barge type floaters have larger pitch motions compared to spar and semi-submersible type floaters. The natural period of the barge type floater in the pitch direction is around 12 s, which coincides with the dominant wave periods, while those of spar-type and semi-submersible type floaters are 36 s and 22 s respectively. (Jonkman, 2007; Kikuchi and Ishihara, 2020). Skirts are used at the platforms in the demonstration projects (FLOATGEN;

NEDO Demonstration Project of Next-Generation Offshore Floating Wind Turbine) to suppress the dynamic responses of floaters, which generate strong nonlinear hydrodynamic forces.

Numerical modeling techniques for floating offshore wind turbine system is categorized into three levels: low-, mid-, and high-fidelity (Otter et al., 2021). Mid-fidelity models, often referred to as engineering-level model or engineering model, are commonly used for dynamic analysis, which is based on equation of motion employing potential-flow theory and Morison's equation. High-fidelity models such as computational fluid dynamic (CFD) is used for detailed investigations of local flow phenomena. In the most comprehensive benchmark study to date named the Offshore Code Comparison Collaboration projects, a three-way validation was conducted between engineering and high-fidelity model and water tank test measurement for semi-submersible type floaters (Benitz et al., 2014). In this paper, the engineering model is applied for dynamic analysis of barge-type floater.

The prediction of hydrodynamic forces is critical for the accurate prediction of the dynamic responses of floating platforms using

---

engineering model. Generally, the linear hydrodynamic forces are evaluated by the potential theory, and the nonlinear hydrodynamic forces are identified from water tank tests. Recently, CFD have been employed to evaluate the nonlinear hydrodynamic forces. Zhang and Ishihara (2018, 2020) employed Large Eddy Simulation (LES) turbulence model with volume of fluid (VOF) method to investigate the hydrodynamic coefficients of multiple heave plates. By using LES, the coherent structures are captured and accuracy is improved, but the subgrid-scale vortices are modeled. Pinguet et al. (2022) predicted the hydrodynamic forces of a thin skirt with a thickness of 1 mm at the bottom of a cylinder by CFD with laminar model in the heave direction. The predicted hydrodynamic forces agreed well with the experiment. He mentioned that a laminar flow assumption could be considered for the boundary layer of the floater when computing the force on the skirt because the generated vortices are large and occur at the edge of the skirt. CFD with fine grids can capture the small vortices well, but the calculation time increases. In order to avoid this, recently, Pan and Ishihara (2019) presented the numerical prediction of hydrodynamic coefficients for a semi-submersible platform using Richardson extrapolation. Numerical errors in the predicted hydrodynamic coefficients by three different grid sizes were systematically studied, the grid independent hydrodynamic coefficients were obtained by Richardson extrapolation, and the extrapolated predictions were validated by the water tank tests. However, the nonlinear hydrodynamic forces of a barge type platform have never been investigated by CFD.

It is well known that nonlinear hydrodynamic coefficients depend on Keulegan-Carpenter (KC) numbers (Graham, 1980). Recently, Gu et al. (2018) investigate the drag, added mass, and radiation damping of cylindrical bodies by CFD for different KC numbers. However, evaluating various hydrodynamic coefficients with different KC numbers needs a high computational cost. Nonlinear hydrodynamic coefficient models are useful, which enable to perform accurate dynamic analysis without high-cost experiments or CFD. Ishihara and Liu (2020) proposed the nonlinear hydrodynamic coefficient model as the function of Reynolds numbers and KC numbers for each component of a semi-submersible platform in the surge and heave directions. The distributed hydrodynamic coefficients in surge and heave directions were integrated to obtain the global coefficient matrix and used for dynamic response analysis of platforms based on the formulas proposed by Ishihara and Zhang (2019). However, the applicability of the hydrodynamic coefficient model on a barge type floater has never been investigated. The hydrodynamic coefficient models need to be validated by comparing with the drag coefficients predicted by CFD for a barge type floater. It also needs to be confirmed whether the drag force in the pitch direction is accurately predicted by the distributed hydrodynamic force in the heave direction or not, since the prediction accuracy of the floater motion in the pitch direction is important for a barge-type floater.

The mean displacement of floater motion has a significant effect on the fatigue lifetime of mooring lines. The offshore oil and gas industry has demonstrated the importance of second-order hydrodynamics, which is solved either directly or with Newman's approximation (Newman, 1974). Bayati et al. (2014) and Pham and Shin (2020) investigated the effects of second-order hydrodynamics on a semi-submersible type floating offshore wind turbine system. The second-order difference-frequency loads improved the prediction accuracy of the drift force for the semi-submersible floaters. Meanwhile, Dev (1996) clarified that the viscous drift force is generated at the splash zone of a wave, where the platform experiences the submerged state at the wave crest and the emerged state at the wave trough, and this force is proportional to the cubic of the wave height. This indicates that the viscous drift force has an impact in the high wave height conditions. Stansberg et al. (2015) reviewed the low-frequency drift force modeling. The full-scale measurement data on the drilling rig of a semi-submersible type platform in the surge direction indicated that Newman's approximation underestimated the measured drift force, which may have caused the two mooring line accidents in

semi-submersible platforms in the oil and gas industry. An empirical adjustment was made on the drift coefficients, especially for the longer wave periods in order to take into account possible contributions from the nonlinear viscous effects and current interactions. However, the influences of the low-frequency drift force due to the nonlinear drag force on the mean floater displacement and mooring tension are not clear yet for the barge-type floater for floating offshore wind turbine systems.

The prediction accuracy of floater motion and mooring tension for semi-submersible type platforms has been improved for the decade. Robertson et al. (2014) compared various existing codes of the engineering model of floating offshore wind turbine systems and pointed out that the prediction accuracy in the pitch direction was improved in the case considering drag force for each element since the effect of off-diagonal terms was included. Ishihara and Zhang (2019) predicted the floater displacement and mooring tension with the proposed correction factors for added mass and drag coefficients used in the augmented Morison's equation. The predicted floater motions and mooring tensions showed good agreement with the measurements. Liu and Ishihara predicted the floater motions in the different wave heights using the proposed hydrodynamic coefficient models considering KC numbers. The predicted floater motions showed good agreement with measurements in both low and high wave height conditions. For barge-type platforms, Kosasih et al. (2019) conducted a comprehensive dynamic analysis using the identified nonlinear drag coefficients from the water tank tests in the regular wave. The predicted surge and heave motions showed good agreement with the measurement, but the predicted pitch motion is overestimated in both low and high wave height conditions. This indicates that the prediction accuracy of dynamic analysis for the barge-type platforms needs to be improved.

In this study, hydrodynamic forces are predicted by CFD, and dynamic responses are investigated by engineering models for a barge-type floater. The fully nonlinear Navier-Stokes/VOF numerical forced oscillation simulations and dynamic analysis using engineering models are described in Section 2. The numerical errors in the predicted hydrodynamic coefficients predicted based on three levels of the grid size are then systematically investigated and the grid-independent hydrodynamic force is evaluated by applying Richardson extrapolation. The applicability of hydrodynamic coefficient models proposed by Ishihara and Liu is investigated for a barge type floater. The global hydrodynamic force in the pitch direction is analytically predicted using the distributed hydrodynamic forces in the heave direction. The effect of drag force on the mean and dynamic response of floater motion and mooring tension are investigated using the engineering model in low and high wave height conditions, in which the validity of the proposed drag force model is also confirmed. Finally, conclusions are given in Section 4.

2. Numerical models

Numerical forced oscillation simulations to evaluate hydrodynamic coefficients are described in section 2.1. The engineering model for dynamic analysis is described in Section 2.2.

2.1. Numerical forced oscillation simulation

Forced oscillation simulations are performed to predict the hydrodynamic coefficients of the barge-type platform. The fully nonlinear Navier-Stokes numerical forced oscillation simulations are conducted within the open-source CFD toolbox OpenFOAM® framework version 1606+ (Weller et al., 1998). The two-phase incompressible Navier-Stokes equations in combination with the Volume of Fluid (VOF) surface capturing scheme developed by Hirt and Nichols (1981) is employed. The governing equations used in the Navier-Stokes/VOF solver, for conservation of mass and momentum of an incompressible flow of air and water are expressed as follows:

$$\nabla \bullet \boldsymbol{u} = 0 \tag{1}$$

$$\frac{\partial \rho \boldsymbol{u}}{\partial t} + \nabla \bullet \left(\rho \boldsymbol{u} \boldsymbol{u}^T\right) = -\nabla p^* - (\boldsymbol{g} \bullet \boldsymbol{x})\nabla \rho + \nabla \bullet \mu\left(\nabla \boldsymbol{u} + (\nabla \boldsymbol{u})^T\right) + f_{\sigma i} \tag{2}$$

where $\nabla = (\partial_x, \partial_y, \partial_z)$ is the three-dimensional gradient operator, $\boldsymbol{u} = (u_1, u_2, u_3)$ is the velocity field in Cartesian coordinates, $\boldsymbol{g}$ is the gravitational acceleration, $\boldsymbol{x} = (x, y, z)$ is the Cartesian coordinate vector, and $f_{\sigma i}$ is the surface tension. p^* is the hydrodynamic pressure, which relates to the total pressure p as below:

$$p^* = p - \rho(\boldsymbol{g} \bullet \boldsymbol{x}) \tag{3}$$

The local density ρ, and the viscosity μ, are defined in terms of the water volume fraction α, formulated as follows:

$$\rho = \alpha \rho_{water} + (1 - \alpha)\rho_{air} \tag{4}$$

$$\mu = \alpha \mu_{water} + (1 - \alpha)\mu_{air} \tag{5}$$

where α is zero for air, one for water and a linear variation for intermediate values. After obtaining the velocity field by solving Eqs. (1) and (2) for the two-phase flow of air and water, the field of α is calculated and advanced in time following the transportation equation of Eq. (6) formulated by Rusche (2003) once the velocity is updated.

$$\frac{\partial \alpha}{\partial t} + \nabla \bullet \boldsymbol{u}\alpha + \nabla \bullet \boldsymbol{u}_r\alpha(1 - \alpha) = 0 \tag{6}$$

Solving the original transportation equation of VOF method would lead to significant smearing of the interface. This is significantly reduced in the formulation by Rusche (2003) by the introduction of an artificial compression term as discussed in Berberović et al. (2009); which is the last term of the left-hand side in Eq. (4). The interface compression term is only active in the vicinity of the interface, i.e. $0 < \alpha < 1$, where its strength is governed by the relative velocity, $\boldsymbol{u}_r$. To ensure the boundedness of α between 0 and 1 in solving the transportation equation in Eq. (6), a multi-dimensional flux limited scheme known as Multidimensional Universal Limited for Explicit Solution (MULES) is used.

The finite volume method is used for discretization, which is based on the application of the conservation principles applied to a finite volume in space known as control volume. For the temporal discretization, i.e., to determine the time step of the numerical simulation, the Courant–Friedrichs–Lewy condition is used. Throughout the present research, a Courant number equal to 0.25 is applied. Table 1 summarizes the numerical schemes used in this research for each term in the governing equation Eq. (1), (2) and (6).

Boundary conditions are set basically according to Pan and Ishihara (2019), and are summarized in Table 2. At the atmosphere boundary of α, the Neumann condition is applied when the fluid flows out of the domain and the Dirichlet condition is applied when the fluid is flowing into the domain. At the seabed boundary, a symmetry (slip) condition is imposed, though the condition does not affect the solution since the water depth is large enough to make the velocity near the seabed negligible. At side walls, symmetry conditions are employed. In general, the no-slip condition requires a finer grid near walls. However, since the side walls are far away from the vibrating platform in this study, the symmetric boundary is used to save computational time and ensure that the velocity component normal to the wall is zero. No-slip condition is

Table 1
Numerical schemes used in this study.

Term		Discretization
Time scheme		Euler, First-order implicit
Spatial gradient scheme		Second-order central difference
Divergence	$\nabla \bullet (\rho \boldsymbol{u})\boldsymbol{u}^T$	First-order upwind
	$\nabla \bullet \boldsymbol{u}\alpha$	MUSCL, Second order TVD
	$\nabla \bullet \boldsymbol{u}_r\alpha(1 - \alpha)$	Interface compression
	$\nabla \bullet \boldsymbol{u}_r\alpha(1 - \alpha)$	Second-order central difference

Table 2
Description of the boundary conditions for volume fraction, hydrodynamic pressure, and velocity.

Items	α	p^*	$\boldsymbol{u}$
Atmosphere	Neumann condition: $\partial\alpha/\partial n = 0$ when the fluid flows out of the domain Dirichlet condition: $\alpha = 0$ when the fluid is flowing into the domain	Dirichlet condition: p = 0	Neumaan condition: $\partial p/\partial n = 0$, Except on the tangential component which is set to 0 for inflow
Seabed	Neumann condition: $\partial\alpha/\partial n = 0$	Neumann condition	Symmetry
Side walls	Symmetry	Symmetry	Symmetry
Inlet and outlet	Neumann condition: $\partial\alpha/\partial n = 0$	Neumann condition: $\partial p/\partial n = 0$	Neumann condition: $\partial u/\partial n = 0$
Structure of platform	Neumann condition: $\partial\alpha/\partial n = 0$	Neumann condition: $\partial p/\partial n = 0$	No-slip wall

applied for the structure of the platform. The predicted viscous shear force integrated over the platform is found to be less than 1% compared to the pressure-derived direct force, and therefore it is considered that the wave radiation and the vortex shedding are dominant to the hydrodynamics compared to the friction.

Reynolds number Re_i for the forced oscillation test in the i direction is defined as below:

$$Re_1 = \frac{(a_1\omega_0)\tau}{v_w}, Re_3 = \frac{(a_3\omega_0)\tau}{v_w}, Re_5 = \frac{(a_5R\omega_0)\tau}{v_w} \tag{7}$$

where i of 1, 3, and 5 corresponds to the direction of surge, heave, and pitch. a_i and $\omega_0 = 2\pi/T_0$ are the prescribed amplitude and angular frequency of the oscillation. T_0 is the oscillation period and v_w is the kinematic viscosity of water. The thickness of the skirt τ is used as the representative length because the skirt is dominant for the flow separation in the forced oscillation in the heave and pitch directions, which is later discussed in Section 3.1. For the pitch direction, the maximum velocity of the front and rear skirts perpendicular to the skirt surface is used as the representative velocity, by multiplying the half-length of the skirt R on the angle amplitude. The Reynolds number in the simulation is 1374 at most, which indicates that the boundary layer remains laminar (e.g., Jensen et al., 1989). It is thus considered that turbulence has a minor effect on the platform loads and laminar model is used for simulations.

The whole computational domain is shown in Fig. 1. The initial conditions for the two-phase flow are set at a water phase depth of 1.0 m and an air phase depth of 0.5 m. The length of the computational domain in the X and Y directions is set as 24.4 m by following the previous paper by Pan and Ishihara (2019), which is a sufficient length to prevent wave propagation from returning to the platform. A structured mesh is used for the discretization of the whole computational domain. The grid size is 0.015 m with the expanding factor from 1.0 to 1.06. In order to resolve the flow separation and deformation of the free surface caused by the
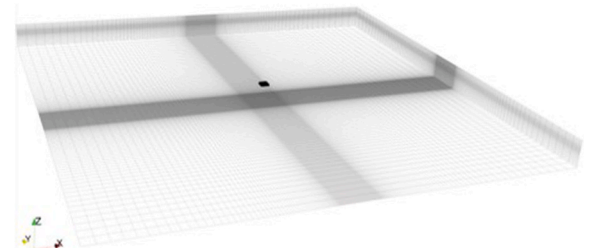

Fig. 1. Computational domain.

platform motion, the castellated mesh is applied in the region near the platform.

The configuration of the 1:100 scale model for the 3 MW barge-type platform and the definition of coordinates are depicted in Fig. 2. The main body of the platform model is a cube with a width of 0.45 m in the X and Y directions and a draft of 0.07 m. A moonpool with a width of 0.27 m is placed in the center of the platform. Skirts with a width of 0.03 m and a thickness of 0.0035 m are attached to the bottom of the platform. The coordinate origin is located at the center of the platform in the X and Y directions and at the free surface in the Z direction. Table 3 shows the main properties of the floater. The center of rotation (CoR) of the forced oscillation equipment in the pitch direction is at 0.0635 m above the water level.

The model is forced to oscillate sinusoidally as shown in Eq. (8) in the still water.

$$x(t) = a \sin(\omega_o t) \tag{8}$$

x and a are the floater displacement and amplitude. To investigate the dependence of the hydrodynamic coefficient on the oscillation period, forced oscillation tests in the surge, heave, and pitch directions are conducted for five periods ranging from 0.8 s to 2.0 s. The time series of hydrodynamic force $F_H(t)$ is obtained by subtracting the buoyancy force F_b and hydrostatic restoring force $F_K(t)$ from the total fluid forces $F_F(t)$ as follows:

$$F_H(t) = F_F(t) - F_b - F_K(t) \tag{9}$$

$$F_b = -\rho_w g \forall \tag{10}$$

$$F_K(t) = -K_R x(t) \tag{11}$$

where ρ_w is the density of water, g is the gravitational acceleration, $\forall$ is the displaced volume of water at the mean position, and K_R is the hydrostatic stiffness. The hydrodynamic force and moment can be decomposed into added mass A and damping N as presented by Eq. (12).

$$F_H(t) = -A\ddot{x}(t) - N\dot{x}(t) \tag{12}$$

The added mass and damping in the i direction, A_{ii} and N_{ii} are obtained by the 1st harmonic components as shown in Eq. (13) and Eq. (14).

$$A_{ii} = \frac{1}{\pi \omega_o a_i} \int_0^{T_o} F_{H11}(t) \sin(\omega_0 t) dt \tag{13}$$

$$N_{ii} = -\frac{1}{\pi a_i} \int_0^{T_o} F_{H11}(t) \cos(\omega_0 t) dt \tag{14}$$

where i is 1, 3 and 5, representing the direction of surge, heave and pitch. The non-dimensional added mass coefficient C_{aii} and damping

Table 3

Dimensions and hydrostatic properties of the 1:100 scale barge type platform model.

Element	Unit	Symbol	Dimension
Width of main body	m	W	0.09
Width of the skirt extended from the main body	m	w	0.03
Area of skirt in X–Y plane	m²	S	0.0576
Draft	m	D	0.07
Freeboard (Elevation of the tower base)	m	b	0.04
Center of rotation (CoR) above the water level	m	C	0.0635
Thickness of skirt	m	τ	0.0035
Displaced volume of water	m³	$\forall$	0.00927
Hydrostatic stiffness in the heave direction	N/m	K_{33}	1270
Hydrostatic stiffness in the pitch direction	Nm/rad	K_{55}	19.5

coefficient C_{Nii} are used to evaluate the added mass and damping as shown in Eqs. (15) and (16).

$$C_{a11} = \frac{A_{11}}{\rho_w \forall}, C_{a33} = \frac{A_{33}}{\rho_w \forall}, C_{a55} = \frac{A_{55}}{I_{55}} \tag{15}$$

$$C_{N11} = \frac{N_{11}}{\rho_w \forall \omega_0}, C_{N33} = \frac{N_{33}}{\rho_w \forall \omega_0}, C_{N55} = \frac{N_{55}}{I_{55} \omega_0} \tag{16}$$

where $\rho_w \forall$ is the mass of displaced volume and I_{55} is the moment of inertia of the platform.

N_{ii} is a composition of the radiation damping N_{rii} proportional to the velocity, and the drag force proportional to the square of velocity as shown in Eq. (17). The drag force needs to be evaluated for dynamic response analysis using engineering model described later in Eq. (28). The radiation damping N_{rii} is obtained from the potential theory by the boundary element method.

$$N_{ii}\dot{x}_i = \left(N_{rii} + \frac{1}{2}C_{dii}\rho_w S |\dot{x}_i(t)| \right) \dot{x}_i(t) \tag{17}$$

where S is the representative area, which is the skirt area in X–Y plane as illustrated in Fig. 2 (a) with gray stitched. The quadratic damping term can be linearized as shown in Eq. (18) (Molin et al., 2007), and the drag coefficients C_{dii} can be derived as Eq. (19).

$$|\dot{x}_i(t)|\dot{x}_i(t) \approx \frac{8}{3\pi}a_i\omega_o\dot{x}_i(t) \tag{18}$$

$$C_{d11} = \frac{N_{11} - N_{r11}}{\frac{4}{3\pi}\rho_w S a_1 \omega_o}, C_{d33} = \frac{N_{33} - N_{r33}}{\frac{4}{3\pi}\rho_w S a_3 \omega_o}, C_{d55} = \frac{N_{55} - N_{r55}}{\frac{4}{3\pi}\rho_w S R^3 a_5 \omega_o} \tag{19}$$

where R is the representative length, which is defined as the half of skirt length 0.255 m.

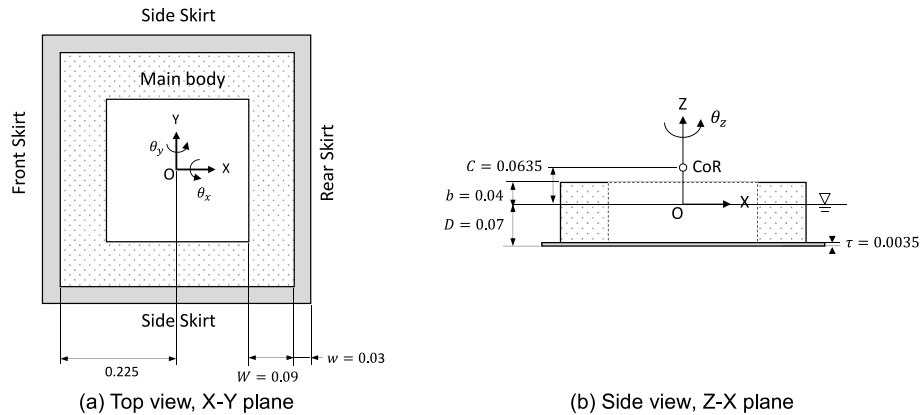The oscillation periods and amplitudes are set as listed in Table 4 in

(a) Top view, X-Y plane   (b) Side view, Z-X plane

Fig. 2. Configuration of the 1:100 scale floater and the definition of coordinates (unit: m).

Table 4

List of cases in the numerical forced oscillation simulations in the 1:100 scale.

Direction	Oscillation Period T_0 [sec]	Amplitude a [m, deg]	KC number KC [-]	Reynolds number Re [-]
Surge	0.8, 1.0, 1.2, 1.5, 2.0	0.01, 0.02, 0.05	0.25, 0.49, 1.23	$110 < Re_1 < 1374$
Heave	0.8, 1.0, 1.2, 1.5, 2.0	0.01, 0.02, 0.03, 0.04	0.25, 0.49, 0.74, 0.99	$110 < Re_2 < 1100$
Pitch	0.8, 1.0, 1.2, 1.5, 2.0	0.5, 3, 5, 10	0.05, 0.33, 0.55, 1.10	$24 < Re_3 < 1223$

order to investigate the period and amplitude dependency of hydrodynamic forces, covering dominant wave periods and wave heights in real sea states. Five different oscillation periods are set to cover dominant wave periods. Reynolds numbers calculated by Eq. (5) are described. Three different amplitudes are set in the surge direction and four different amplitudes are set in the heave and pitch directions in order to clarify the dependency of hydrodynamic forces on the KC number. The KC number in the surge, heave, and pitch directions are calculated by Eq. (36), Eq. (37) and Eq. (41) as defined later in Section 3.1.

The systematic errors of the predicted hydrodynamic coefficients are investigated using three different refinement levels of grid. An approximate solution is obtained using the fine grid and the grid independent solution is then estimated by Richardson extrapolation. The exact solution φ is assumed as Eq. (20) expressed as the sum of the approximate solution φ_h with a grid size of h and the corresponding discretization error ε_h. When the grid is fine enough, ε_h is proportional to the main term of the Taylor series, as expressed as Eq. (21). α is a derivative and is independent of h, the exponent p is the order of the numerical scheme, and H is the higher order term.

$$\varphi = \varphi_h + \varepsilon_h \tag{20}$$

$$\varepsilon_h \approx \alpha h^p + H \tag{21}$$

The exponent p and α can then be derived by the solutions on the three grid levels as Eqs. (22 and 23), where λ means the ratio of grid sizes and $h_1 = \lambda h_2 = \lambda^2 h_3$. In general, p is 1 when the first order scheme is used for time discretization and the grid velocity is constant. However, as pointed out by Pan and Ishihara (2019), p can be less than 1 when the dynamic mesh with a variable grid velocity is used.

$$p = \frac{\log\left(\frac{\varphi_{h_2} - \varphi_{h_1}}{\varphi_{h_3} - \varphi_{h_2}}\right)}{\log \lambda} \tag{22}$$

$$\alpha = \frac{\varphi_{h_3} - \varphi_{h_2}}{h_3^p(\lambda^p - 1)} \tag{23}$$

The exact solution is obtained as Eq. (24) based on the solution φ_{h_i} with the grid size of h_i.

$$\varphi = \varphi_{h_i} + \alpha h_i^p + H \tag{24}$$

Once p is identified, the discretization error on the second grid ε_h can be derived as Eq. (25) using solutions of two different grid levels φ_{h_1} and φ_{h_2}. Finally, the exact solution is obtained as Eq. (26).

$$\varepsilon_{h2} \approx \alpha h^p = \frac{\varphi_{h_2} - \varphi_{h_1}}{\lambda^p - 1} \tag{25}$$

$$\varphi = \varphi_{h_2} + \frac{\varphi_{h_2} - \varphi_{h_1}}{\lambda^p - 1} \tag{26}$$

Three levels of grids are built to perform Richardson extrapolation as shown in Fig. 3. The finest grid is used in the area at a distance of 2τ from the surface of the platform. The second finest grid is used for the boxed area covering 0.045 m from the tip of the skirt, based on the visualization of the vortices and the free surface deformation, which is discussed later in Section 3.1. The number of cells is 4.9 million for the level 1 grid, 8.5 million for the level 2 grid, and 40.9 million for the level 3 grid.

2.2. Engineering modeling for dynamic analysis

The dynamic response of the motion and mooring tension are evaluated by OrcaFlex 11.2 d. The platform and tower are modeled as a single point of mass with mooring restraints. The nonlinear equation of motion for the platform point of mass is written as Eq. (27):

$$M\{\ddot{x}\} + C\{\dot{x}\} + K\{x\} = \{F_G\} + \{F_B\} + \{F_K\} + \{F_H\} + \{F_E\} + \{F_{ED}\} + \{F_M\} \tag{27}$$

where $\{x\}$, $\{\dot{x}\}$, and $\{\ddot{x}\}$ are displacement of the platform in 6DoF and their time derivatives; M, C, and K represent the mass, damping, and stiffness matrix. $\{F_G\}$, $\{F_B\}$, $\{F_K\}$, $\{F_H\}$, $\{F_E\}$, $\{F_{ED}\}$, and $\{F_M\}$ denote the gravitational, buoyancy, hydrostatic restoring, hydrodynamic, linear wave excitation, 2nd order wave drift, and mooring restraint forces. The hydrostatic restoring force $\{F_K\}$ is obtained by Eq. (11). The hydrodynamic forces $\{F_H\}$ in the numerical model can be written as a sum of the hydrodynamic inertia force $\{F_A\}$, linear radiation damping force $\{F_r\}$, and drag force $\{F_D\}$ as shown in Eq. (28). Hydrodynamic inertia force and linear radiation damping force relates with added mass A and radiation damping N_r as shown in Eqs. (29 and 30). The 6DoF matrices of A and N_r are obtained from the potential-flow analysis, where the commonly used boundary element method is used by the computer program ANSYS AQWA. For the dynamic response simulations, the frequency-dependent added mass and radiation damping in the time domain is calculated by the Cummins equation. Drag force $\{F_D\}$ is calculated based on the member-level model, known as Morison element as described in Section 2.3.

$$\{F_H\} = \{F_A\} + \{F_r\} + \{F_D\} \tag{28}$$

$$\{F_A\} = -A\{\ddot{x}\} \tag{29}$$

$$\{F_r\} = -N_r\{\dot{x}\} \tag{30}$$

The drag coefficient is implemented as Morison elements. In the model, the drag force normal to each element f_D with area dS is
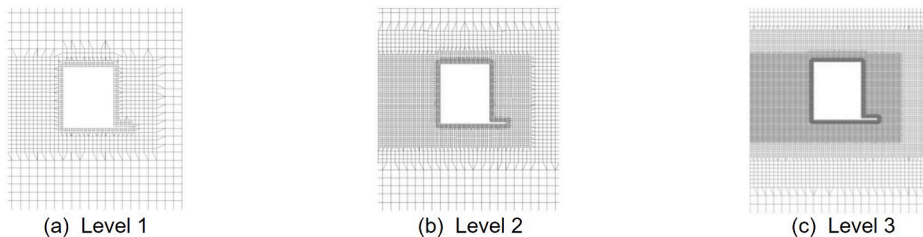

(a) Level 1   (b) Level 2   (c) Level 3

Fig. 3. The Z-X plane view of the grid around the model for each refinement level.

calculated by Eq. (31), where v_X and v_n are the velocity of the skirt and its component normal to the skirt. C_d is determined from the drag co-efficient model proposed in Section 3.1.

$$f_D = \frac{1}{2}\rho_w C_d v_X |v_n| \, dS \tag{31}$$

The diffraction analysis of linear potential theory provides the 6DoF vectors of linear wave excitation force $\{F_E\}$ as the sum of the 1st order Froude-Krylov and diffraction forces. $\{F_E\}$ is represented by frequency-dependent force amplitude per wave amplitude $\{f_{E,n}\}$ and phase $\varphi_{E,n}$ as a summation of each wave component n as shown in Eq. (32).

The wave drift force $\{F_{ED}\}$ in the surge direction is considered by Newman's approximation of the quadratic transfer function (QTF) matrices calculated by the second-order potential theory using the wave amplitude a_n and the diagonal component of the QTF $\{Q_n\}$ for each wave component as shown in Eq. (33).

$$\{F_E\} = \sum_{n=1}^{N} a_n \{f_{E,n}\} \sin(\omega_{E,n}t - \varphi_{E,n}) \tag{32}$$

$$\{F_{ED}\} = \sum_{n=1}^{N} a_n^2 \{Q_n\} \tag{33}$$

Mooring restraint force $\{F_M\}$ is calculated by the finite element model. The added mass coefficient and drag coefficient of mooring lines in the normal direction $_{mooring}C_a^n$ and $_{mooring}C_d^n$ are set as 1.0 and 1.2 respectively referring to Ishihara and Zhang (2019) that used the same studless chains in the experiments shown later in Section 3.2. Morison's equation is used to evaluate the dynamic loading on each segment.

In free decay tests and simulations, the natural period and the damping ratio in the surge and pitch directions are investigated by sampling ten peaks of the displacement from the static equilibrium position $a_{p,1}, a_{p,2}, ..., a_{p,10}$, excluding the initial value $a_{p,0}$. The average period from the 1st peak to the 10th peak is taken as the natural period, and the average of damping ratio ξ_n calculated by Eq. (34) is taken as the damping ratio.

$$\xi_n = -\frac{1}{4\pi} \log\left(\frac{a_{p,n+2}}{a_{p,n}}\right) \tag{34}$$

3. Results and discussions

In Section 3.1, hydrodynamic coefficients for a barge-type platform are numerically predicted by different grid refinement levels in the surge, heave, and pitch directions. The influence of grid refinement is systematically studied, and grid independent solution is obtained by applying Richardson extrapolation. The applicability of the hydrodynamic coefficient model on barge-type floater is investigated. In Section 3.2, dynamic analysis is conducted and the effect of drag force on the mean floater displacement and mooring tension is investigated. In Section 3.3, the effect of drag force on the dynamic response of floater motion and mooring tension is investigated.

3.1. Hydrodynamic force assessment by CFD simulation

Water tank tests for the forced oscillation are conducted with a 1:100 scale model for the barge type platform at the current water tank of Mitsui Akishima Laboratory in order to measure hydrodynamic forces for the validation of the predicted ones by CFD. The forced oscillation tests are performed as Fig. 4. The length, width and depth of water tank are 100 m, 5 m and 2.65 m respectively. The platform is attached to the forced oscillation equipment. The forces and moment in surge, heave and pitch directions are measured using a 3-component force transducer installed on the forced oscillation equipment at 0.1885 m above the water plane. The displacement is measured by the laser displacement meter.

The experiment cases are listed in Table 5. In order to see the dependency of wave periods, 5 oscillation periods from 0.8 to 2.0 s is conducted with the amplitude of 0.05 m in surge, 0.04 m in heave and 5° in pitch direction. In order to see the dependency of wave height, 0.02 m in surge and heave directions and 3° in pitch direction is conducted with 1.2 s.

Hydrodynamic forces are analyzed from the measured sinusoidal forces using Eqs. 8–19 and the added mass coefficient and damping coefficient are obtained. The measured force includes the effect of the oscillation equipment. The inertia and damping forces of the equipment is separately measured by performing a forced oscillation test of the equipment in the air for each oscillation period and amplitude. The fluid force F_F in Eq. (9) is evaluated by subtracting the inertia of the platform model and equipment F_I and the damping force of the oscillating device ΔF_D for each oscillation period and amplitude.

$$F_F(t) = F(t) - F_I(t) - \Delta F_D(t) \tag{35}$$

Numerical forced oscillation simulations configured in Section 2.1 are conducted firstly with an oscillation period of 1.2 s and an amplitude of 0.04 m conducted with the level 1, level 2, and level 3 grids. The time history of hydrodynamic force in the heave direction measured and simulated with level 2 grid is presented in Fig. 5.

The amplitude of hydrodynamic force $F_H(t)$ is calculated as 31.78 N in level 1 grid, 31.21 N in level 2 grid and 30.85 N in level 3. By using Eq. (22), the parameter of Richardson extrapolation p is evaluated as 0.67. For hydrodynamic forces of other periods and amplitudes in surge, heave and pitch directions, p of 0.67 and the predicted hydrodynamic forces with level 1 and level 2 grids are used in Eq. (26).

Figs. 6–8 show variation of the predicted added mass and damping coefficients with the grid size in surge, heave and pitch directions

Table 5
List of cases in the forced oscillation experiment.

Period [s]	Surge amplitude a_1 [m]	Heave amplitude a_3 [m]	Pitch amplitude a_5 [deg]
0.8, 1.0, 1.2, 1.5, 2.0	0.05	0.04	5
1.2	0.02	0.02	3

(a) Surge direction   (b) Heave direction   (c) Pitch direction

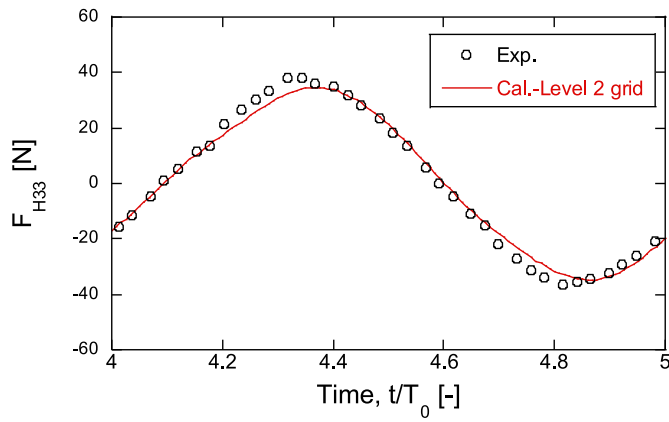**Fig. 4.** Water tank tests for the forced oscillation.

Fig. 5. Comparison of measured and predicted hydrodynamic forces in the heave direction with $T_0 = 1.2$ s and $KC_3 = 0.99$.

analyzed by Eqs. (13) and (14). Table 6 shows the predicted added mass and damping coefficients with different grid size and its error compared to the experiments. The predicted added mass in the surge and pitch direction and the predicted damping coefficients in the surge and heave direction by the level 1 grid show good agreement with the measurements and weak grid dependence. The added mass coefficient in the heave direction predicted with the level 2 grid underestimates the measurements with the error of -8.5%, but the added mass coefficient predicted by Richardson extrapolation agreed well with the measurements with the error of -3.3%. The damping coefficient in the pitch direction predicted with the level 2 grid underestimates the measurements with the error of -18.3%, but the damping coefficient predicted by Richardson extrapolation shows good agreement with the measurements with the error of -4.0%. As a result, Richardson extrapolation improves the prediction accuracy for the added mass coefficient in the heave direction and the damping coefficient in the pitch direction. The accuracy of the forced oscillation is validated since the predicted hydrodynamic forces with Richardson extrapolation matches well with the measured ones.
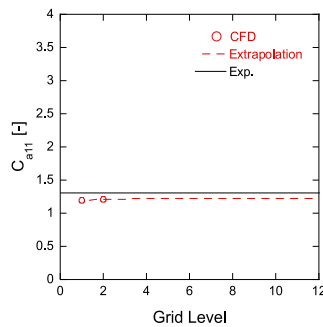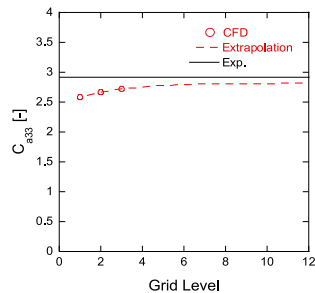

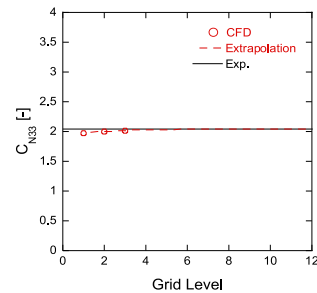
(a) Added mass coefficient C_{a11}
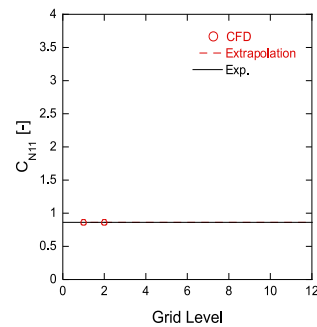
(b) Damping coefficient C_{N11}

Fig. 6. Variation of the predicted hydrodynamic coefficients with the different grid size in the surge direction with $T_0 = 1.2$ s and $KC_1 = 1.23$.
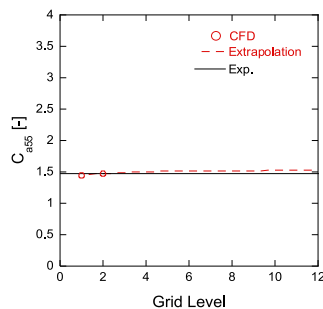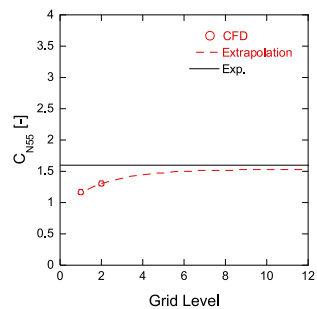

(a) Added mass coefficient C_{a33}

(b) Damping coefficient C_{N11}

Fig. 7. Variation of the predicted hydrodynamic coefficients with the different grid size in the heave direction with $T_0 = 1.2$ s and $KC_3 = 0.99$.

(a) Added mass coefficient C_{a55}

(b) Damping coefficient C_{N55}

Fig. 8. Variation of the predicted hydrodynamic coefficients with the different grid size in the pitch direction with $T_0 = 1.2$ s and $KC_5 = 0.55$.

Table 6
The predicted added mass and damping coefficients with different grid size and its error compared to experiment.

|		Exp.	Level 1	(Error)	Level 2	(Error)	Extrapolation	(Error)
Added mass coefficient in the surge direction	C_{a11}	1.304	1.202	(-7.8%)	1.210	(-7.2%)	1.225	(-6.1%)
Damping coefficient in the surge direction	C_{N11}	0.862	0.867	(0.6%)	0.866	(0.5%)	0.866	(0.5%)
Added mass coefficient in the heave direction	C_{a33}	2.913	2.583	(-11.3%)	2.666	(-8.5%)	2.816	(-3.3%)
Damping coefficient in the heave direction	C_{N55}	2.036	1.976	(-2.9%)	1.997	(-1.9%)	2.049	(0.6%)
Added mass coefficient in the pitch direction	C_{a55}	1.480	1.445	(-2.4%)	1.474	(-0.4%)	1.523	(2.9%)
Damping coefficient in the pitch direction	C_{N55}	1.598	1.171	(-26.7%)	1.306	(-18.3%)	1.534	(-4.0%)
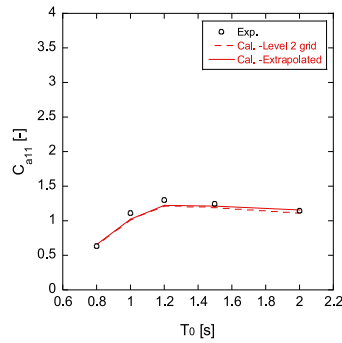
(a) Added mass coefficient C_{a11}
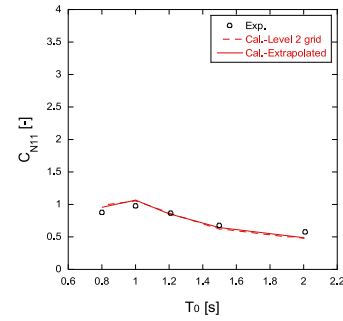

(b) Damping coefficient C_{N11}

Fig. 9. The hydrodynamic coefficient predicted by the grid level 2 and Richardson extrapolation in the surge forced oscillation with KC = 1.23 for the five oscillating periods.

Forced oscillation simulations in the surge direction are conducted. The predicted added mass and damping coefficients are presented in Fig. 9. Dash line shows the prediction with the level 2 grid and the solid line represents the results obtained by Richardson extrapolation. The added mass and damping coefficients predicted by the level 2 grid and Righardson extrapolation show good agreement with the measurements for all oscillation periods within 7% error. Vorticity is visualized by the Q-criterion as shown in Fig. 10 (a) and (b) in order to clarify the flow
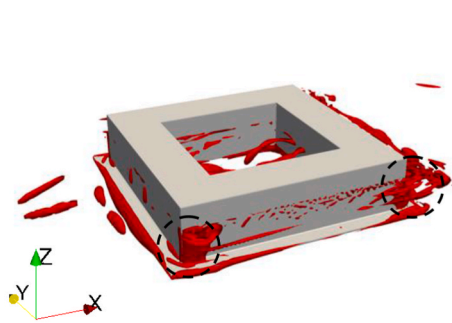
(a) Bird view of vorticity at Q-Criterion=20
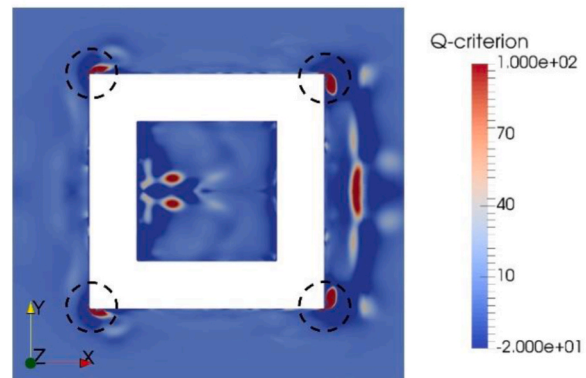
(b) Top view of vorticity (X-Y plane at the half draft)
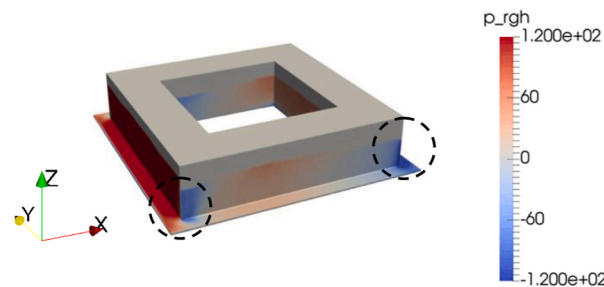
(c) Brid view of hydrodynamic pressure

Fig. 10. Contour of vorticity and hydrodynamic pressure in the forced oscillation simulation in the surge direction. ($a_1 = 0.05$ m, $T_0 = 1.2$ s, t = 4.5T_0, when platform velocity is maximum in the negative direction).

characteristic. It is observed that the flow separation occurs at the corner of the main body, which is the area enclosed by the dashed circle. Fig. 10 (c) shows that the hydrodynamic pressure is significantly decreasing in the wake of the corners of the main body, although the hydrodynamic pressure on the negative X side of the floater is mostly positive due to wave radiation. This result indicates that the horizontal drag coefficient in the engineering model discussed in Section 3.3 needs to be distributed at the corner of the main body.

Forced oscillation simulations in the heave direction are conducted. The predicted added mass and damping coefficients are presented in Fig. 11. The experiment value of 0.8 s is removed because it is considered inaccurate. The added mass coefficients predicted by the grid level 2 slightly underestimate the measurement data, while those predicted by Richardson extrapolation agree well with measurements. The mean error for all simulations performed was reduced from 7% to 2% by Richardson extrapolation. The measured added mass in 1.5 s might have an experimental error. The damping coefficients predicted by the grid level 2 and Richardson extrapolation agree well with the measurements in the oscillation periods of more than 1.2 s. In the oscillation periods less than 1.0 s, the predictions overestimate the measurements, since it is considered that the quipment attached on top of the platfrom model may be interfering with the oscillation of the water surface in the moonpool. Vorticity is visualized by Q-criterion as shown in Fig. 12 (a) and (b) in order to clarify the flow characteristic. The flow separation occurs at the tip of skirts, which is the area enclosed by the dashed circle. Fig. 12 (c) shows that the hydrodynamic pressure is decreasing in the wake of the skirt. This result indicates that the vertical damping coefficient needs to be distributed at the skirt in the dynamic analysis discussed in Section 3.3.

Forced oscillation simulations in the pitch direction are conducted. The predicted added mass and damping coefficients are presented in Fig. 13. The added mass coefficients predicted by the grid level 2 and Richardson extrapolation agree well with the measurements in all oscillation periods within 5% error. The damping coefficients predicted by grid level 2 underestimate the measurement data, while those predicted by Richardson extrapolation agree well with measurement. The mean error for all simulations performed significantly decreases from 21% to 7% using Richardson extrapolation. Vorticity is visualized by the Q-criterion as shown in Fig. 14 (a) and (b) in order to clarify the flow characteristic. The flow separation occurs at the tip of the skirts, which is the area enclosed by the dashed circle. The size of the vortex corresponds to the amplitude of the oscillation, and it can be seen that the closer to the center of rotation, the smaller the size of the vortex at the skirt. Fig. 14 (c) shows that the hydrodynamic pressure decreases corresponding to the flow separation at the skirt.

The drag coefficients are evaluated by Eq. (19). The relationship between the drag coefficient and KC number is investigated. KC number is a nondimensional value calculated as the ratio of the oscillation amplitude to the representative length of the floater. Here R is the half

length of the skirt 0.255 m. The equation of KC numbers in the surge and heave direction are summarized as follows:

$$KC_1 = \frac{2\pi a_1}{R} \tag{36}$$

$$KC_3 = \frac{2\pi a_3}{R} \tag{37}$$

The predicted drag coefficients with different KC numbers are plotted in Fig. 15. The drag coefficient exhibits a decreasing trend as KC number increases in both surge and heave directions. This relationship has been reported in studies investigating sharp-edged bodies (Graham, 1980; Ishihara and Liu, 2020). In the surge direction, the drag coefficient shows a weak decrease with increasing KC number. This is because the drag force is primarily affected by the larger diameter main body. On the other hand, in the heave direction, the drag coefficient shows a significant decrease with increasing KC numbers. This is because the drag force is largely affected by the thinner skirt. Also, it is observed that the drag coefficient in the surge direction decreases with longer periods, whereas the drag coefficient in the heave direction generally did not depend on the period.

The drag coefficient models of barge-type floater in the surge and heave directions are proposed by Eqs. (38) and (39), based on the drag coefficient model proposed by Ishihara and Liu (2020) for square cylinder components of semi-submersible floaters. Here the coefficients of KC γ_1 and γ_3 are introduced. These parameters are 1 in Ishihara and Liu (2020), but they are identified as 2.83 for γ_1 and 28.3 for γ_3 in this study. The differences in γ_1 and γ_3 are due to the difference in the dimension of R in Eqs. (36) and (37). The dimensionless parameter ξ_1 represents the dependence on the wave period. In the surge direction, ξ_1 is fitted as a function of the dimensionless period T_* and T_{Ref} is a reference period of 12s in full scale. $C_{d11,ref}$ and $C_{d33,ref}$ are the drag coefficients in the surge and heave directions for the cases with amplitude of 0.02 m as shown in Table 4.

$$C_{d11} = C_{d11,ref}\left\{ -0.45(\gamma_1 KC_1 + 1)^{0.33} + 1.93 \right\}\xi_1, \gamma_1 = 2.83,$$
$$\xi_1 = e^{-c_1\left(T_*^{0.8} - 1\right)}\left(c_1 = T_{Ref}^{0.8}, T_* = T\Big/ T_{Ref}\right) \tag{38}$$

$$C_{d33} = C_{d33,ref}\left\{ -0.45(\gamma_3 KC_3 + 1)^{0.33} + 1.93 \right\}, \gamma_3 = 28.3 \tag{39}$$

Fig. 16 shows the distributed hydrodynamic coefficients on each Morison element, which is determined by the visualization result in Figs. 10 and 12. Surge drag coefficients are distributed at the corner of the main body and heave drag coefficients are distributed at the edge of the skirt. The global drag coefficient in the pitch direction is analytically calculated from the distributed drag coefficient in the heave direction predicted by the model as shown in Eq. (37) and compared with that predicted by the numerical prediction.

The drag coefficient for each Morison element at the distance X from
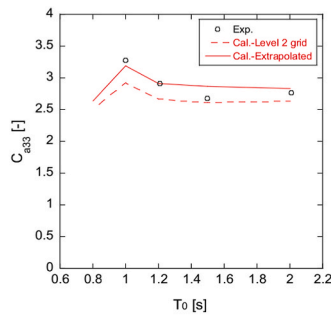
(a) Added mass coefficient C_{a33}
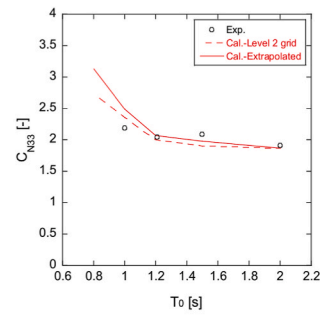
(b) Damping coefficient C_{N33}

Fig. 11. The hydrodynamic coefficient predicted by the grid level 2 and Richardson extrapolation in the heave forced oscillation with KC = 0.99 for the five oscillating periods (0.04 m).
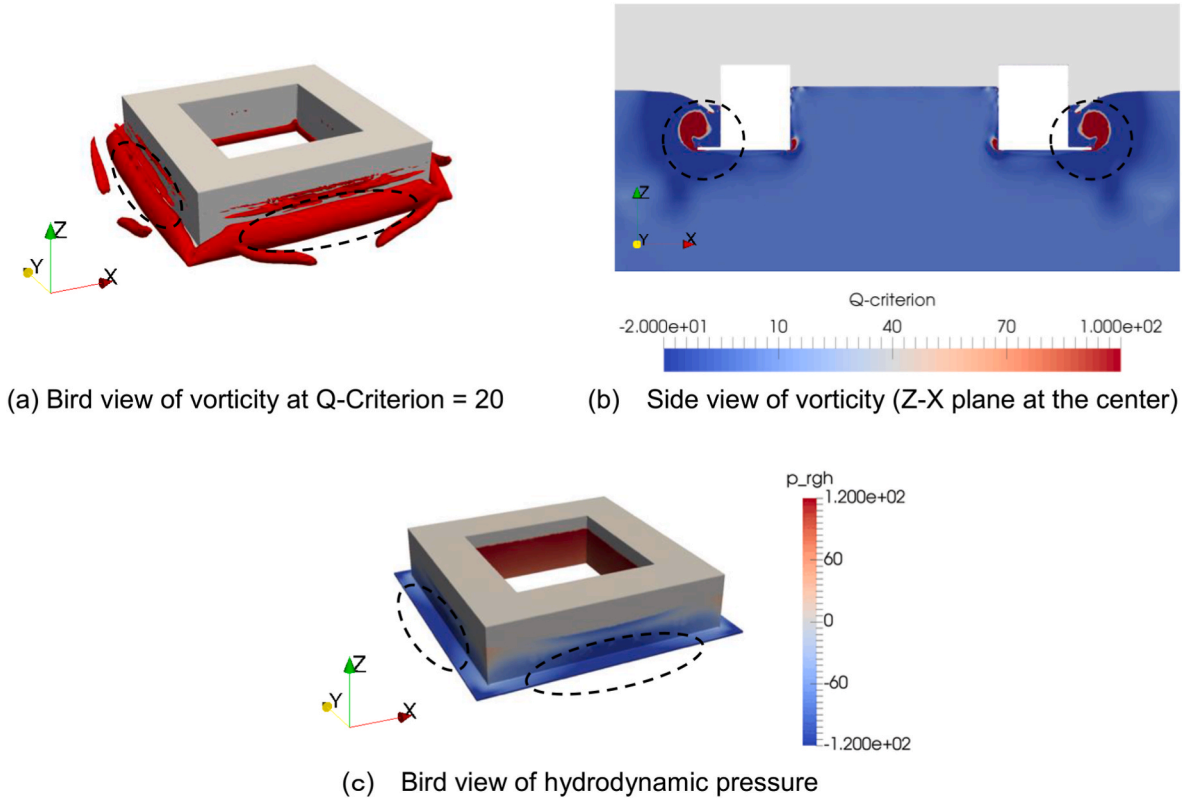
(a) Bird view of vorticity at Q-Criterion = 20

(b) Side view of vorticity (Z-X plane at the center)

(c) Bird view of hydrodynamic pressure

Fig. 12. Contour of vorticity and hydrodynamic pressure in the forced oscillation simulation in the heave direction. (a_3 = 0.04 m, T_0 = 1.2 s, t = 4.5T_0, when platform velocity is maximum in the negative direction).

(a) Added mass coefficient C_{a55}
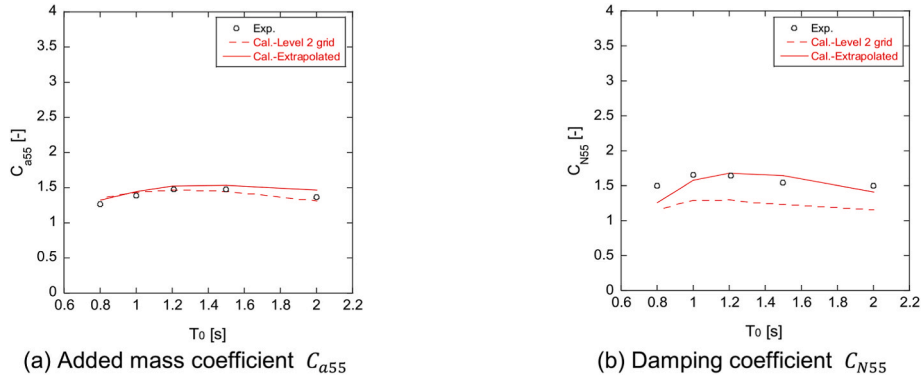

(b) Damping coefficient C_{N55}

Fig. 13. The hydrodynamic coefficient predicted by the grid level 2 and Richardson extrapolation in the pitch forced oscillation with KC = 0.55 for the five oscillating periods (5 deg amplitude with respect to CoR).

the origin is defined as $C_{d33,Skirt}(X)$ as shown in Eq. (40), which is derived from the drag coefficient model in the heave direction. The KC number at each element is calculated as shown in Eq. (41). Here, Xa_5 is the arc amplitude in the normal direction of the skirt. X is the distance from the center of the skirt calculated by Eq. (42) as a function of the local co-ordinate along the skirt l. l varies along the side skirt.

$$C_{d33,Skirt}(X) = C_{d33}(KC_3(X)) \qquad (40)$$

$$KC_3(X) = \frac{2\pi(Xa_5)}{R} \qquad (41)$$

$$X = \begin{cases} |l| & side\ skirt \\ R & front\ skirt, rear\ skirt \end{cases} \qquad (42)$$

The drag force of each Morison element f_D due to the pitch motion is

calculated by Eq. (43), where v_X and v_n are the velocity of the skirt and its component normal to the skirt. In the forced oscillation in the pitch direction, the time series of v_X and v_n are respectively calculated by Eqs. (44) and (45). Here, L is the distance from the CoR to the skirt.

$$f_D(X) = \frac{1}{2}\rho_w C_{d33,Skirt}(X)v_X|v_n|w\,dl \qquad (43)$$

$$v_X = -a_5\omega_0\sqrt{X^2 + L^2}cos(\omega_0 t) \qquad (44)$$

$$v_n = -a_5\omega_0 X\,cos(\omega_0 t) \qquad (45)$$

The global moment in the pitch direction F_{D55} is calculated from the drag force of each Morison element f_D as shown in Eq. (46). The first and second terms correspond to the contribution of two side skirts, and the third and fourth terms to that of front and rear skirts. The drag
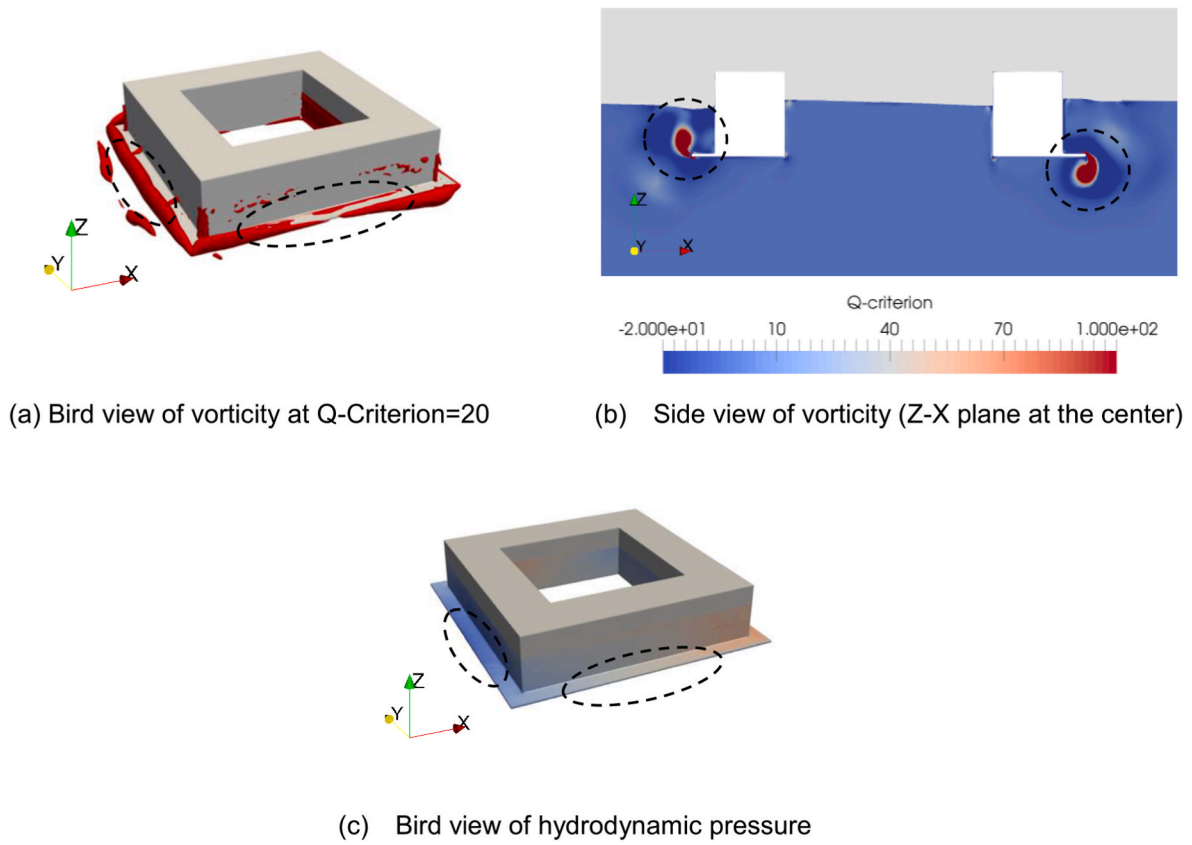
(a) Bird view of vorticity at Q-Criterion=20

(b) Side view of vorticity (Z-X plane at the center)

(c) Bird view of hydrodynamic pressure

Fig. 14. The contour of vorticity and hydrodynamic pressure in the forced oscillation simulation in pitch direction. ($a_5 = 5$ deg, $T_0 = 1.2$ s, $t = 4.5T_0$, when platform velocity is maximum in the negative direction).
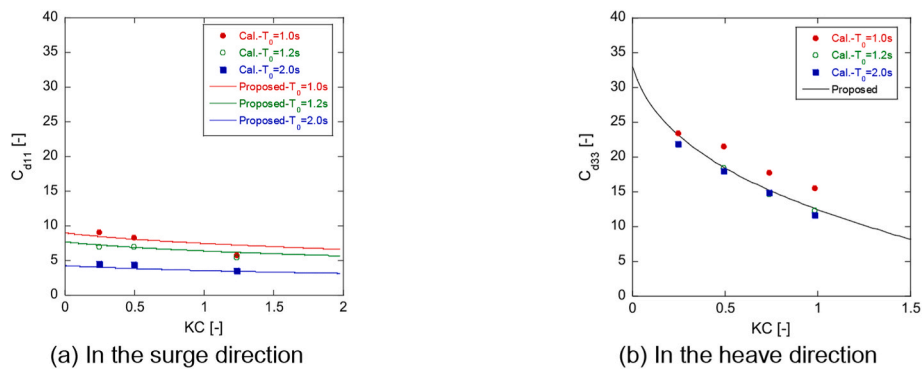

(a) In the surge direction

(b) In the heave direction

Fig. 15. Comparison of predicted drag coefficients by the proposed model and those from the numerical simulation.
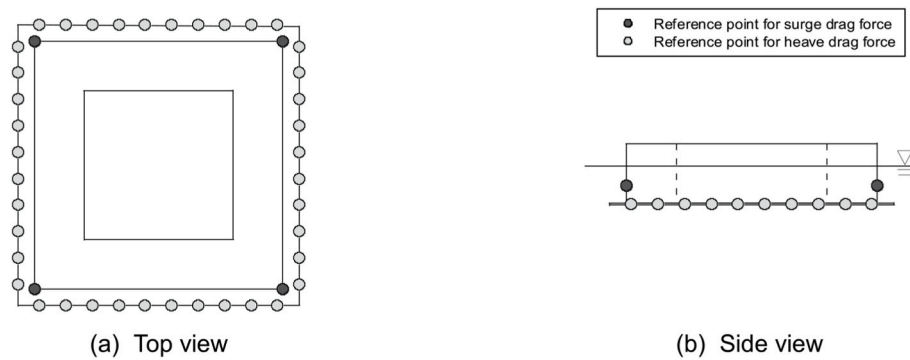

(a) Top view

(b) Side view

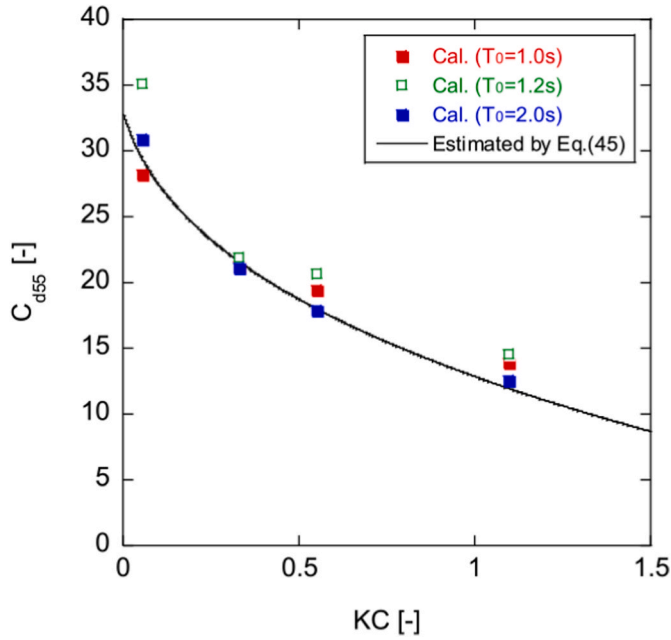**Fig. 16.** Distributed drag force in surge and heave directions on each Morison element.

Fig. 17. Comparison of the predicted drag coefficient C_{d55} by the distributed the drag force in the heave direction and those from the numerical simulation.

coefficient in the pitch direction C_{d55} can be derived as shown in Eq. (47). The hydrodynamic force in the surge direction is negligible to calculate the global force in the pitch direction because the distance between the force and the center of rotation is short.

$$F_{D55} = \int_{-R_2}^{R_2} X f_D(X) w \, dl + \int_{-R_2}^{R_2} X f_D(X) w \, dl + \int_{-R_2}^{R_2} R f_D(R) w \, dl$$
$$+ \int_{-R_2}^{R_2} R f_D(R) w \, dl \tag{46}$$

Fig. 17 shows the comparison of global drag coefficient in the pitch
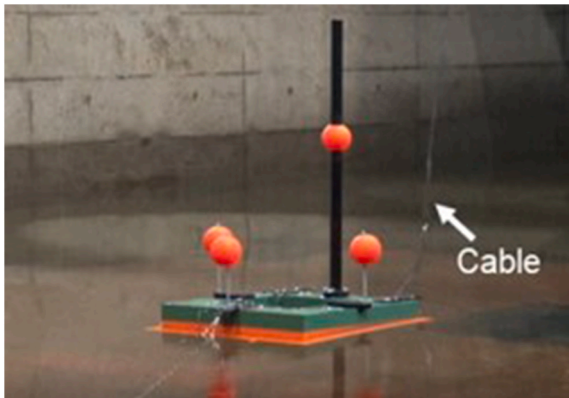

Fig. 18. Overview of the dynamic response test.

direction C_{d55} calculated by Eq. (47) and those from the numerical simulation. It is found that the predicted drag coefficients in the pitch direction from the distributed drag coefficients in the heave direction show good agreement with those from the numerical simulations. The drag coefficient in the pitch direction significantly decreases as the KC number increases. This indicates that the drag coefficient model in the heave direction can be used to predict the drag force in the pitch direction at the same time. Only the drag coefficient models in the surge and heave directions are used as the inputs and the drag force in the pitch direction is automatically calculated to predict the dynamic response of the floater.

3.2. The effect of hydrodynamic force on the mean displacement of floater

To validate the performance of the engineering model using the proposed nonlinear hydrodynamic coefficient models, the dynamic response experiments of a 1:100 scale model for the 3 MW barge-type floater are conducted in the small towing tank of Mitsui Akishima Laboratory. The dimensions of the water tank are 55 m in length, 8 m in width, and 1 m in the water depth. Fig. 18 presents the overview of the dynamic response test. The floater motion is measured by an optical motion capture camera. Three optical targets on the deck of the platform and one in the middle of the tower are installed to capture the 6DoF platform motion. The cable is attached to the freeboard of the platform to transmit the information of the measured mooring tension, which affected the initial displacement in the pitch direction. The incoming wave is measured by the wave probe placed upstream of the floater at X = −7.39 m and Y = 0.0 m.

The floater model is the same as the forced oscillation test model described in Table 3. The tower is only installed in the dynamic response experiment with a mass of 1.4 kg and a height of 0.7 m. Four catenary mooring lines, i.e., ML1 to ML4, are installed as shown in Fig. 19. Mooring lines are installed at an angle of 20° to the X-axis, and are connected to the fairlead located at X = −0.265 m, Y = ±0.0 m and Z = 0.04 m for ML1 and ML2 and at X = −0.265 m, Y = ±0.18 m, and Z = 0.04 m for ML3 and ML4. Each mooring line is 9.86 m length. The

$$C_{d55} = \frac{\int_0^{T_o} F_{D55} dt}{\int_0^{T_o} \frac{1}{2} \rho_w S R^3 |\dot{x}_5(t)| \dot{x}_5(t) dt} = \frac{\int_{-R_2}^{R_2} C_{d33,Skirt}(X) X^3 w \, dl + \int_{-R_2}^{R_2} C_{d33,Skirt}(R) \sqrt{R^2 + L^2} R^2 w \, dl}{\frac{1}{2} S R^3} \tag{47}$$

studless chains as shown in Fig. 20 are used and the properties of the chain are given in Table 7. The displacement of the floater is 9.27 kg including the mass of the floater, the mass of optical targets, the mass of tower, and the apparent mass of mooring lines in water. The center of gravity and the moment of inertia are measured to be located at 0.055 m and 0.3555 kgm^2 above the water plane, considering the platform, optical targets and tower mass.

The dynamic analysis is conducted using the engineering model described in Section 2.2. Drag coefficients in the horizontal and vertical directions are calculated from the hydrodynamic models proposed in the previous section. Drag coefficients in the vertical direction consider the amplitude at each Morison element as shown in Eqs. (38)–(40). Simulation cases of dynamic analysis are summarized in Table 8. Case 1 is a static equilibrium test conducted to confirm the initial position of the floater and the fairlead tension in the mooring lines. Case 2 is free decay test to evaluate the natural period and the damping ratio of the floater in the surge, heave, and pitch directions. Case 3 is the regular wave test, where two conditions are set for wave height H, one for the low wave height condition of 0.02 m and the other for a high wave height condition of 0.18 m. For the low wave condition, wave period T_0 is set in the
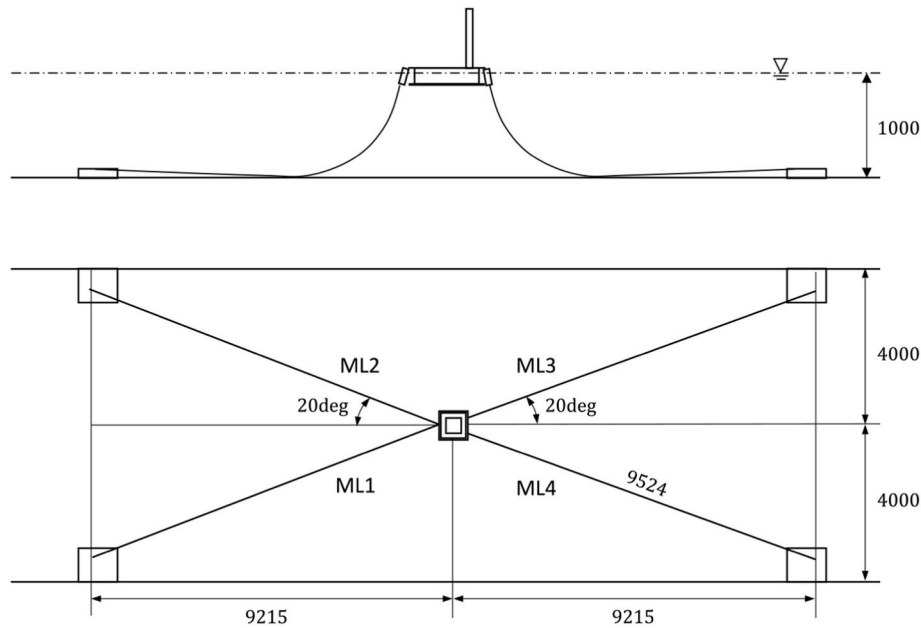
Fig. 19. Top and side view of the mooring system. (units: mm).

(a) Overview of chain

(b) Schematic chain and notations

Fig. 20. Configuration of chain used for mooring lines.

Table 7
Chain properties in mooring system.

Material	Nominal diameter d_m (mm)	Length P_m (mm)	Spacing W_m (mm)	Weight in the air (N/m)	Weight in water (N/m)
Steel	3	24	5	1.432	1.246

Table 8
Simulation cases.

Cases	Condition	Description
1	Still water	Static equilibrium test
2	Still water	Free decay test in the surge, heave, and pitch directions
3	Regular wave	(a) Low wave, T_0 = 0.8–1.8 s, H = 0.02 m; (b) High wave, T_0 = 1.2–1.8 s, H = 0.18 m
4	Irregular wave	(a) Low wave, T_s = 1.4 s, H_s = 0.02 m; (b) High wave, T_s = 1.4 s, H_s = 0.10 m

Table 9
The initial displacement of the floater in the static equilibrium test in each direction.

Item	Measurement	Prediction	Error
Surge	−0.0026 m	−0.0026 m	0%
Heave	0 m	0 m	0%
Pitch	1.1 deg	1.1 deg	0%
Mooring tension in ML1	3.78 N	3.78 N	0%
Mooring tension in ML3	3.72 N	3.72 N	0%

range from 0.8 s to 1.8 s. For high wave conditions, T_0 is set in the range from 1.2 s to 1.8 s, which does not exceed the theoretical wave breaking limit. Case 4 is the irregular wave test. Pierson-Moskowitz spectra are set as a target of wave generation, with a significant wave period T_s = 1.4 s. Two conditions for significant wave height H_s are set, one for the low wave height condition of H_s = 0.02 m and the other for the high wave height condition of H_s = 0.10 m. A unidirectional wave is generated to propagate along the positive X axis.

The measured and predicted initial displacements are summarized in Table 9. Due to the cable for measuring the mooring tension, the initial displacement of 1.1 deg in the pitch direction is observed. Instead of modeling the cable, the coordination of the center of gravity is shifted to 5.8 mm in the X direction to reproduce this initial displacement. The length of mooring lines ML1 and ML2 is shortened by 5.5 mm, or 0.06% of the total length to reproduce the measured initial mooring tension of ML1 and ML2. The angle of mooring lines ML3 and ML4 from the X axis is adjusted from 20.0 deg to 20.88 deg to reproduce the measured initial mooring tension of ML3 and ML4.

The measured and predicted time series of floater motion in free decay simulation are depicted in Fig. 21. The initial displacements are −0.087 m, −0.029 m, and 5.4 deg in the surge, heave, and pitch direction. The drag coefficient was determined by Eqs. (38) and (39), based on the KC values evaluated from the initial displacements of each Morison element shown in Fig. 16, and the natural period iteratively obtained from the simulation. The predicted time series presented an excellent agreement with the experiment for the surge, heave, and pitch directions. The natural periods and damping ratio are analyzed as shown in Fig. 22. The predicted natural periods match the measured ones for all models within 6% or less errors. In the heave direction, two-peak phenomena are observed as a composite of two oscillation periods around
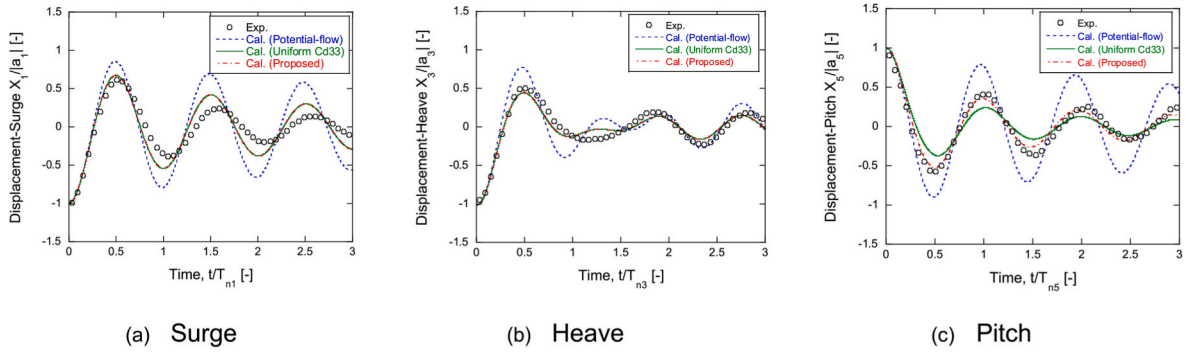
Fig. 21. Comparison of measured and predicted floater displacement in free decay simulations.
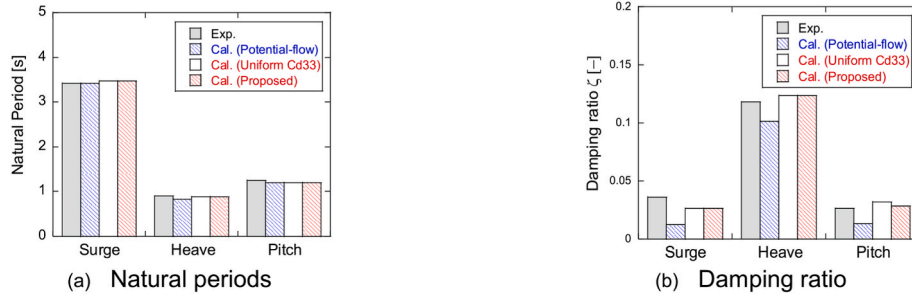

Fig. 22. Comparison of measured and predicted natural periods and damping ratio.

0.72 s and 1.0 s. The resonance period and the damping ratio are tentatively calculated from the initial displacement and the first peak. The predicted damping ratios by the potential flow model underestimate the measured values, while the predictions by the proposed model show good agreement with the measurements. The prediction errors reduce from 66% to 38% in the surge direction, from 16% to 5% in the heave direction, and from 49% to 7% in the pitch direction. In the pitch direction, the damping ratio using a uniform vertical hydrodynamic coefficient is overestimated by 21%, while the damping ratio predicted using the distributed vertical hydrodynamic coefficient agrees well with the measurements and the prediction error reduces to 7%. This indicates that considering the distribution of drag coefficients improves the accuracy of floater motion in the pitch direction.

As mentioned by Stansberg et al. (2015), two accidents occurred in the oil and gas industry due to the insufficient consideration of the mean drag force effect on the mooring lines of semi-submersible floaters. To explain how the drag force produces a mean floater displacement in the surge direction as derived by Dev (1996), the kinetic theory of regular waves is incorporated using the airy wave theory as shown in Eq. (48).

$$\eta = \eta_a \cos(\omega_o t), u_x = \eta_a \omega_o \cos(\omega_o t) \qquad (48)$$

where η is the surface elevation, u_x is the corresponding velocity of the water particles of the wave head, and η_a is the wave amplitude. The drag force per unit length $\Delta F_D(t)$ on a floating cylinder with diameter D in regular waves can be expressed with the drag coefficient C_d and the relative velocity u_r as shown in Eq. (49). The relative velocity u_r is the difference between the water particle velocity u_x and the floater velocity in the surge direction, which can be expressed as a sinusoidal function with amplitude of u_{ra} and phase advance $\varepsilon_{u_r\dot{x}}$ from the water particle velocity as follows:

$$\Delta F_D(t) = \frac{1}{2}\rho_w C_d D u_r |u_r| \qquad (49)$$

$$u_r(t) = u_{ra} \cos(\omega_o t + \varepsilon_{u_r\dot{x}}) \qquad (50)$$

Substituting Eq. (48) into Eq. (47), $\Delta F_D(t)$ is obtained as follows:

$$\Delta F_D(t) = \frac{1}{2}\rho C_d u_{ra}^2 D\Delta z \cos(\omega_o t + \varepsilon_{u_r\dot{x}})|\cos(\omega_o t + \varepsilon_{u_r\dot{x}})|$$

$$\sim \frac{4}{3\pi}\rho C_d D\Delta z \omega_0^2 \eta_a^2 \cos(\omega_o t + \varepsilon_{u_r\dot{x}}) \qquad (51)$$

Eq. (51) indicates that the drag force produces a zero mean force on a part of the platform submerged over the entire period, and that the in-phase portion of the drag force with the crest velocity can create the mean force in the wave splash zone, in which the part is not always submerged. A mean component in the splash zone of the drag force $F_{D0}(t)$ is found by integrating the unit length force over the splash zone as follows:

$$F_{D0}(t) = \int_0^{T_0} \int_{z=0}^{z=\eta_{ra}} \Delta F_D(t) dt \qquad (52)$$

where η_{ra} is the free surface elevation relative to the floater obtained from the difference between the free surface elevation and the heave motion of the floater is expressed as a sinusoidal function with amplitude of η_{ra} and phase advance $\varepsilon_{\eta,z}$ from the free surface elevation as shown in Eq. (53).

$$\eta_r(t) = \eta_{ra} \cos(\omega_o t + \varepsilon_{\eta_r z}) \qquad (53)$$

Finally, a mean component of the viscous drag force $F_{D0}(t)$ can be analytically calculated by Eq. (54).

$$F_{D0}(t) = \frac{4}{3\pi}\rho C_d D\omega_0^2 \eta_a^2 \frac{1}{T_0}\int_0^{T_0}$$

$$\times \int_0^{z=\eta_{ra}} \cos(\omega_o t + \varepsilon_{u_r\dot{x}}) dz dt = \frac{2}{3\pi}\rho C_{d0} D\left(\frac{2\pi}{T_0}\right)^2 \eta_{ra}^3 \cos(\varepsilon_{\eta_r z} - \varepsilon_{u_r\dot{x}}) \qquad (54)$$
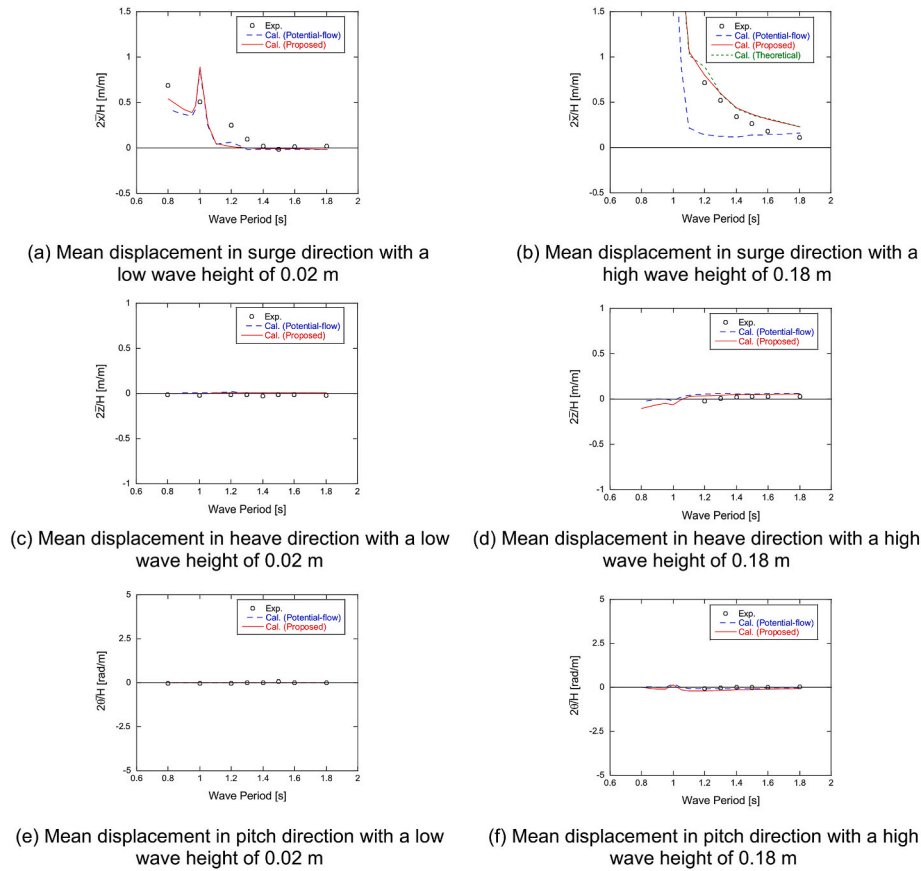
Fig. 23. The predicted and measured mean floater displacement in regular waves.

It is derived that the mean drag force is proportional to the cubic of the wave height and inversely proportional to the square of the wave frequency. The increase in mean displacement leads to an increase in the maximum value of mooring tension. This indicates that the mean drag force is important to accurately predict the maximum value of mooring tension in the high wave height condition.

Fig. 23 shows the predicted mean displacements with and without

consideration of the nonlinear drag force coefficients for the low wave height of 0.02 m and the high wave height of 0.18 m. In the case of low wave height, the predicted mean displacements with and without consideration of nonlinear drag force coefficients are nearly equal as shown in Fig. 23 (a). This is because the wave drift QTF, which is proportional to the square of the wave height, dominates the mean displacement at small wave height, rather than the mean drag force
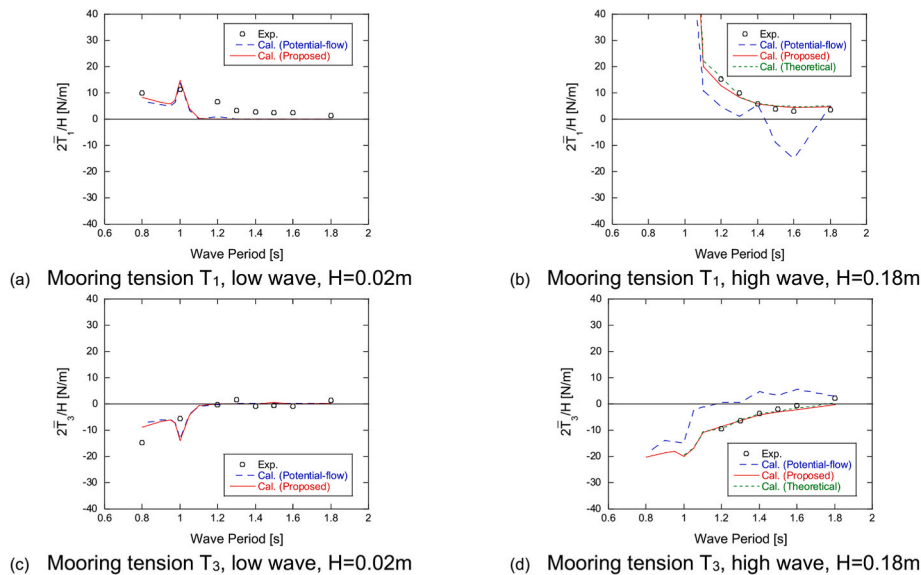

Fig. 24. The predicted and measured mean mooring tensions in regular waves.

which is proportional to the cube of the wave height. Although there are some discrepancies between the experimental and predicted values, the predictions capture the tendency of surge mean displacement to increase on the side of shorter periods where the wave drift QTF is larger. The peak at the wave period of 1.0 s corresponds to the heave natural period. Molin and Lacaze (2016) analytically showed that the surge wave drift force QTF is coupled with the heave motion of the floater in the second order potential theory. The simulated QTF shows the peak at the natural period in the heave direction, though the measured QTF does not have this peak as reported by Tan et al. (2021). Further research is required to accurately evaluate the wave drift force QTF. On the other hand, for the high wave height case, the predicted mean displacement in the surge direction without the nonlinear drag force significantly underestimates the measurements as shown in Fig. 23 (b), while those with the nonlinear drag force show good agreement with the measurements and increase with the cube of the wave frequency as expected by Eq. (54). The error of mean surge displacement at 1.2 s is reduced from 81% to 12% using the proposed drag model. The mean displacement is also predicted by considering a mean component of the viscous drag force theoretically calculated by Eq. (52) instead of considering drag coefficients. The predicted mean surge displacement is consistent with that predicted by considering drag force, which also confirms that the mean displacement comes from the drag force. The mean displacements in the heave and pitch directions are sufficiently small compared to the mean displacement in the surge direction and the amplitude of dynamic

response discussed later for both low and high wave height conditions.

The predicted mean mooring tensions of mooring lines 1 and 3 are plotted in Fig. 24. The mooring tension increases with shorter wave periods, which corresponds to the surge mean displacement. In the low wave height condition, the predicted mooring tension by the potential theory and the proposed drag force coefficients show good agreement with measurement. However, in the high wave height case, the predicted mooring tension by the potential theory significantly underestimates the measurement for the mooring line 1 and overestimates that for the mooring line 3, since the predicted surge displacement by the potential theory obviously underestimates the measurement, while the predicted mooring tensions by the proposed model show good agreement with the measured ones. The error at 1.2 s is reduced from 69% to 9% for mooring line 1, and from 105% to 0% for mooring line 3. It is also confirmed that the theoretical drag force can explain the influence of drag force coefficients on the mooring tensions.

3.3. The effect of hydrodynamic force on the dynamic response of floater

The dynamic response of the floater is calculated using the proposed drag force coefficient models. The predicted and measured RAOs in both low and high wave heights are plotted in Fig. 25. In the low wave height case, the predicted floater displacements without considering nonlinear drag force overestimate the measured values in the resonance region around 1.0 s in the heave direction and 1.2 s in the pitch direction. On

(a) Surge direction, low wave, H=0.02 m

(b) Surge direction, high wave, H=0.18 m

(c) Heave direction, low wave, H=0.02 m

(d) Heave direction, high wave, H=0.18 m

(e) Pitch direction, low wave, H=0.02 m
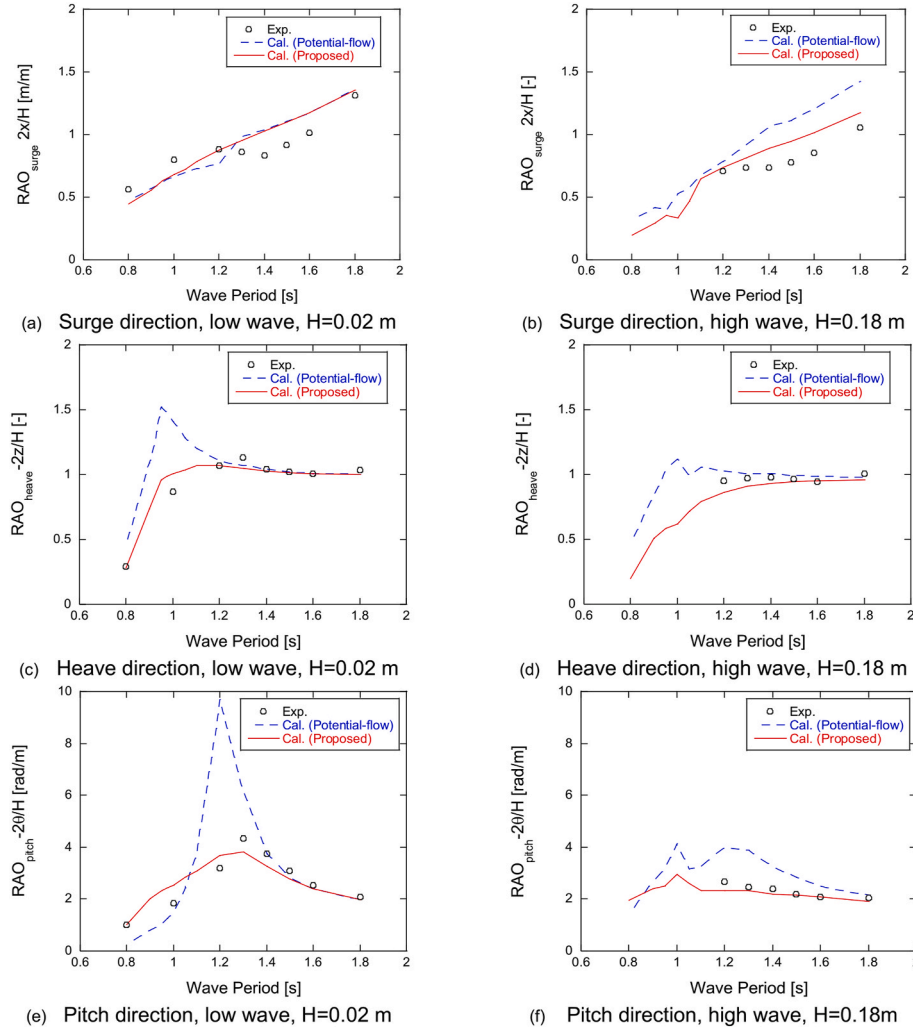
(f) Pitch direction, high wave, H=0.18m

Fig. 25. The predicted and measured RAO of the floater motions in regular waves.
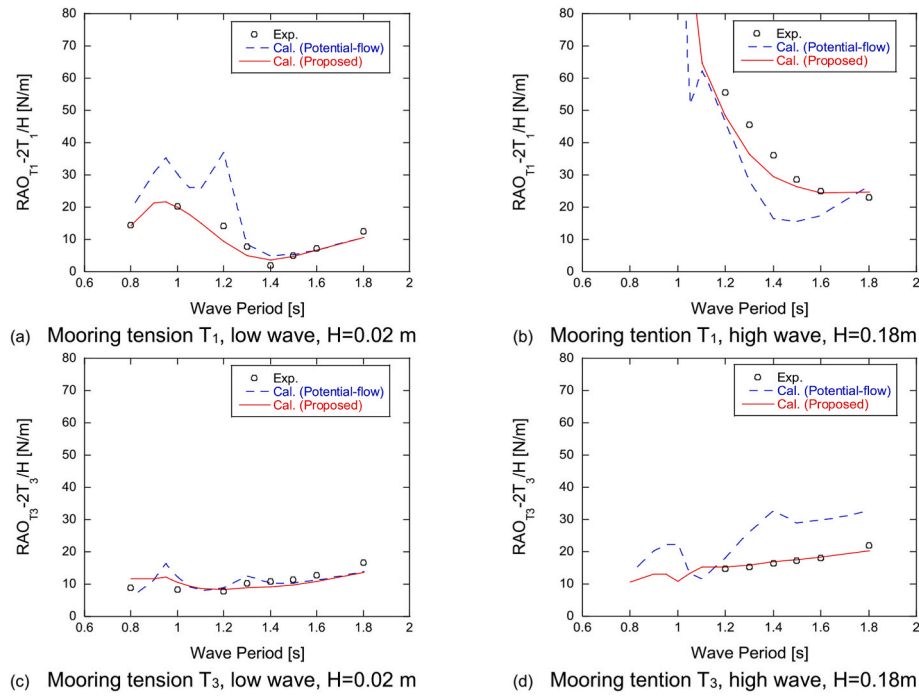
Fig. 26. The predicted and measured RAO of mooring tension in regular waves.

the other hand, when considering nonlinear drag force, the predictions show good agreement with the measurements. The error reduced from 32% to 27% for heave resonant response and from 200% to 20% for pitch resonant response.

In the high wave height case, the predicted floater displacement by potential theory overestimates the measurements in the surge direction for periods longer than 1.3 s, as well as in the pitch direction around the resonant period of 1.2 s. It is also observed that the heave resonance affects the pitch displacement. On the other hand, the predicted floater displacements using the proposed hydrodynamic coefficient model demonstrate good agreement with the measurements. The overestimation in the surge direction around 1.4 s has decreased from 44% to 20%, and the error in the pitch direction at the resonant period of 1.2 s has reduced from 50% to 13%.

The measured and predicted mooring tensions are plotted in Fig. 26. Fig. 26(a) illustrates the mooring tension of mooring line 1 in the low wave height. The predictions based on potential theory significantly overestimate the measurements in the resonance regions of 1.0 s in the heave direction and that of 1.2 s in the pitch direction. It suggests that the prediction of mooring tension is affected by the floater motion when hydrodynamic forces are not accurately considered, which is not

observed in the case of a semi-submersible floater. In the high wave height, the predicted mooring tension of mooring line 1 by the potential theory underestimates the measurements and that of mooring line 3 overestimates the measurements. This is a combined effect of the overestimation in surge and pitch floater motions by the potential-flow model. The predicted mooring tensions by the proposed hydrodynamic force model show good agreement with the measurements for both mooring line 1 and line 3 in low and high wave heights. The errors for line 1 in the low wave height case have reduced from 48% to 4% at 1.0 s and from 160% to 30% at 1.2 s. Additionally, in the case of high wave height, the errors have decreased from 55% to 18% for line 1 and from 99% to 3% for line 3 respectively at 1.4 s.

Irregular wave simulations are performed using the proposed drag coefficient model. The measured and simulated significant wave heights are shown in Fig. 27. The measured time series of significant wave height is directly inputted in the simulation, and so the measured and simulated wave spectrum perfectly matches.

Amplitudes to evaluate hydrodynamic coefficients in Eqs. (38) and (39) are identified from Eq. (55), using the power spectral density of the relative velocity in the normal direction of each Morison element S_{V_r} and the corresponding angular frequency ω. The natural preriod in the surge
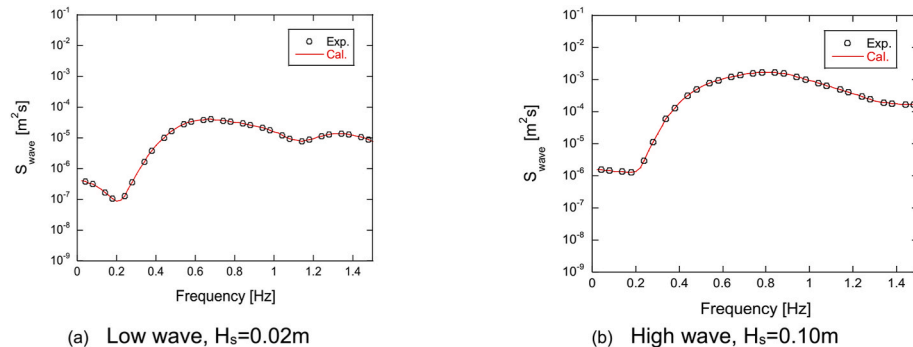

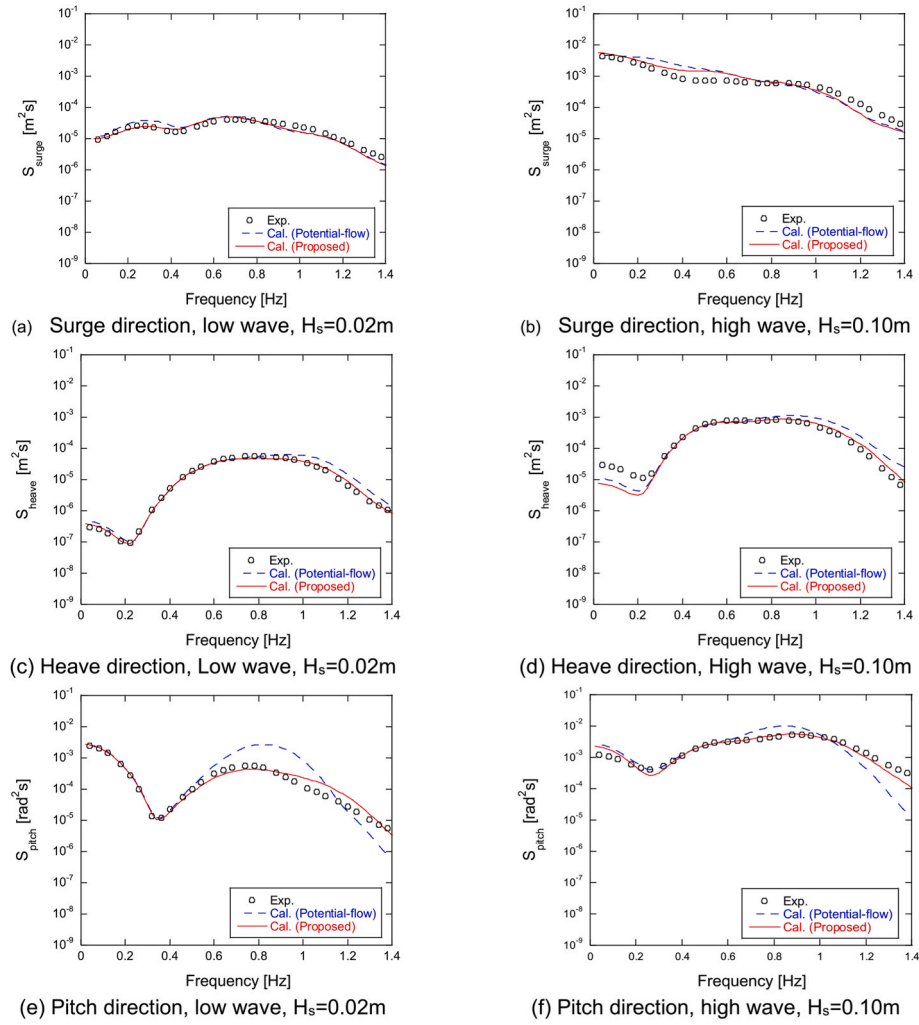**Fig. 27.** The power spectrum of the incoming irregular waves.

Fig. 28. The measured and predicted power spectrum of the dynamic response of the floater in irregular waves.

direction is used for the wave period to evaluate the drag coefficients in surge direction in Eq. (38).

$$a_i = \sqrt{\int_0^\infty \frac{S_{V_r,i}(\omega)}{\pi\omega^2} d\omega} \tag{55}$$

The response spectra of the floater motion for low and high wave heights are presented in Fig. 28. In the low wave height case, the predictions by the potential-flow model overestimate the measurements in the resonance regions of 0.3 Hz in the surge direction, 1.1 Hz in the heave direction, and 0.8 Hz in the pitch direction. Otherwise, the proposed model shows good agreement with the measurements in those resonance regions. The mean component in the pitch direction is attributed to the measurement cable. In the high wave height condition, the predictions by the potential theory underestimate the measurements in the resonance regions of 1.1 Hz in the heave direction and 0.8 Hz in the pitch direction as same as the low wave height case, though the proposed model shows good agreement with the measurements. The peaks around low frequencies of 0 Hz and 0.3 Hz correspond to the drift and surge natural frequencies.

The response spectra of the mooring tension are shown in Fig. 29. In the low wave height case, the predictions by the potential flow model

are overestimated for both mooring lines 1 and 3 in the pitch resonance frequencies. This result coincides with the overestimation of mooring tension predicted by the potential flow model in the surge and pitch resonance regions in regular wave simulation. The predictions by the proposed model agree well with measurements, which also coincides with the predictions in regular wave simulation. In the high wave height case, the predictions by the potential flow model overestimate the measurements for all wave frequencies, while the predictions by the proposed model match well with the measruements. The peak at the low frequency of 0 Hz corresponds to the drift in the surge direction.

For quantitative comparisons, the measured and predicted standard deviations for low and high wave height conditions are shown in Fig. 30 and the prediction errors are summarized in Tables 10 and 11. In the low wave height case, the prediction errors decrease from 7.9% to −0.7% in the surge direction, from 6.8% to −3.7% in the heave direction, and from 109.1% to −1.7% in the pitch direction. In the high wave height case, the prediction errors also decrease from 18.3% to 7.4% in the surge direction, from 6.3% to −3.4% in the heave direction, and from 23.9% to −2.5% in the pitch direction. For the mooring tensions, the proposed model also improves the prediction accuracy of the standard deviation in both low and high wave height conditions, except for the mooring tension ML3 in the low wave height case. These results are consistent
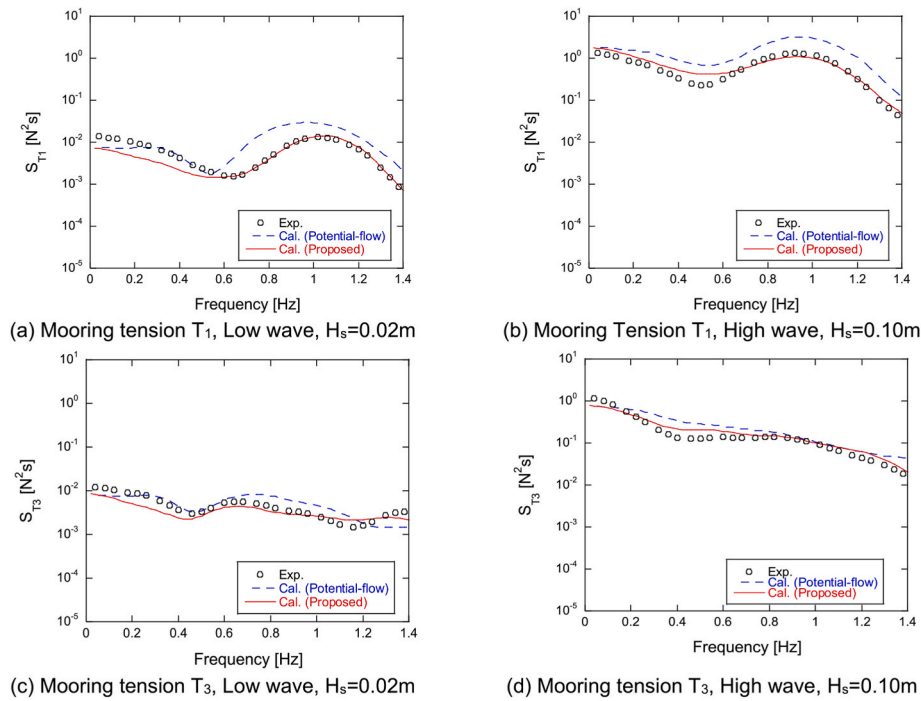
Fig. 29. The measured and predicted power spectrum of mooring tension in irregular waves.
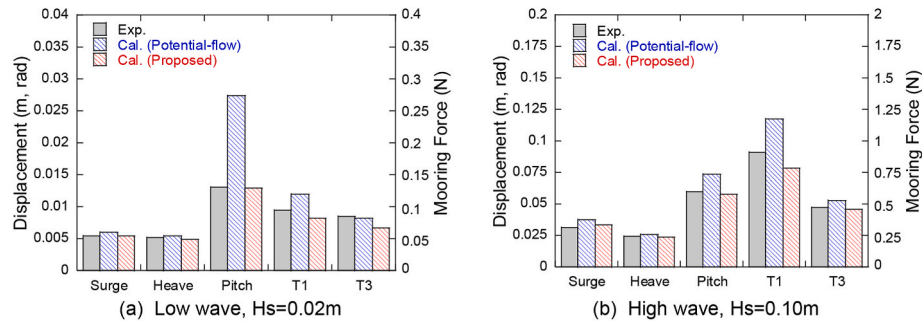

Fig. 30. The measured and predicted standard deviation in irregular waves.

Table 10
The measured and predicted standard deviations in the irregular wave at the low wave height condition (Hs = 0.02 m).

Item	Measurement	Potential-flow (Error)	Proposed (Error)
Surge [m]	0.00549	0.00592 (+7.9%)	0.00545 (−0.7%)
Heave [m]	0.00509	0.00544 (+6.8%)	0.00491 (−3.7%)
Pitch [rad]	0.00131	0.00274 (+109.1%)	0.00129 (−1.7%)
Tension ML1 [N]	0.0943	0.1190 (+26.0%)	0.0814 (−13.7%)
Tension ML3 [N]	0.0846	0.0821 (−3.0%)	0.0666 (−21.4%)

Table 11
The measured and predicted standard deviation in the irregular waves at the high wave height condition (Hs = 0.10 m).

Item	Measurement	Potential-flow (Error)	Proposed (Error)
Surge [m]	0.0315	0.0373 (+18.3%)	0.0339 (+7.4%)
Heave [m]	0.0245	0.0260 (+6.3%)	0.0236 (−3.4%)
Pitch [rad]	0.0595	0.0738 (+23.9%)	0.0580 (−2.5%)
Tension ML1 [N]	0.911	1.171 (+28.5%)	0.785 (−13.9%)
Tension ML3 [N]	0.472	0.526 (+11.6%)	0.456 (−3.2%)

with the RAOs obtained from the regular wave tests and the improvement is particularly notable in the pitch direction with a 100% improvement in accuracy for the low wave height case and a 20% improvement for the high wave height case. These improvements indicate that the effects of the drag coefficient in the surge and heave directions are significant in the prediction of floater motion.

4. Conclusions

Hydrodynamic forces and dynamic responses of a barge-type floater are investigated using CFD and engineering model. The conclusions are obtained as follows:

1. The grid-independent added mass and damping coefficients are obtained by Richardson extrapolation and are validated by water tank tests. It is clarified that the flow separation occurs at the corner of the main body in the surge direction and at the tips of the skirts in the heave direction by visualization of vorticity. It is shown that the existing drag coefficient models as a function of the KC number are applicable for the barge-type floater. The global hydrodynamic coefficient in the pitch direction predicted by the distributed hydrodynamic coefficients in the heave direction matches well with that predicted by CFD.

2. The predicted mean values of surge and mooring tension show a good agreement with the measurements in the high wave height condition by considering the nonlinear drag force, while those without consideration of the nonlinear drag force coefficient underestimate the measurement. It is analytically shown that the mean drag force is inversely proportional to the square of the wave period and proportional to the cube of wave height, which is also confirmed by dynamic analysis considering nonlinear drag force coefficients.

3. The predicted dynamic responses of floater and mooring tension show good agreement with the measurements in the low and high wave height conditions, while those without consideration of the nonlinear drag force overestimate the measurements at the frequencies of heave and pitch. The predicted mooring tensions by the potential theory are overestimated or underestimated in heave and pitch directions, while the predicted ones by the proposed drag force model show good agreement with the measurements. This indicates that the mooring tension is significantly affected by the floater motion. The predicted dynamic responses of floater and mooring tension in irregular waves show a good agreement with the measurements in the low and high wave height as a result of correctly considering both mean and dynamic components.

CRediT authorship contribution statement

Hiromasa Otori: Investigation, Data curation, Visualization, Writing – original draft. **Yuka Kikuchi:** Conceptualization, Resources, Writing – review & editing. **Irene Rivera-Arreba:** Software, Writing – review & editing. **Axelle Viré:** Resources, Writing – review & editing.

Declaration of competing interest

The authors declare that they have no known competing financial interests or personal relationships that could have appeared to influence the work reported in this paper.

Data availability

The authors do not have permission to share data.

References

ANSYS Inc, 2019. AQWA. R1.

Bayati, I., Jonkman, J., Robertson, A., Platt, A., 2014. The effects of second-order hydrodynamics on a semisubmersible floating offshore wind turbine. J. Phys. Conf. 524, 012094 https://doi.org/10.1088/1742-6596/524/1/012094.

Benitz, A.M., Schmidt, P.D., Matthew, L.A., Stewart, G.M., Jonkman, J., Robertson, A., 2014. Comparison of hydrodynamic load predictions between reduced order engineering models and computational fluid dynamics for the OC4-DeepCwind semi-submersible. In: Proceedings of the ASME 2014 33rd International Conference on Ocean, Offshore and Arctic Engineering, ume 9B. Ocean Renewable Energy. V09BT09A006. San Fransisco, California, USA. https://doi.org/10.1115/OMAE2014-23985.

Berberović, E., van Hinsberg, N.P., Jakirlić, S., Roisman, I.v., Tropea, C., 2009. Drop impact onto a liquid layer of finite thickness: dynamics of the cavity evolution. Phys. Rev. E - Stat. Nonlinear Soft Matter Phys. 79 https://doi.org/10.1103/PhysRevE.79.036306.

Hywind Demo. https://www.equinor.com/news/archive/2009/09/08/InnovativePowerPlantOpened. (Accessed 7 January 2023).

Dev, A.K., 1996. Viscous Effects in Drift Forces on Semi-submersibles. PhD Thesis. Delft University of Technology, Delft, The Netherlands.

FLOATGEN. https://floatgen.eu/. (Accessed 7 January 2023).

Fukushima FORWARD. http://www.fukushima-forward.jp/english/index.html. (Accessed 7 January 2023).

Graham, J.M.R., 1980. The forces on sharp-edged cylinders in oscillatory flow at low Keulegan-Carpenter numbers. J. Fluid Mech. 97 (2), 331–346. https://doi.org/10.1017/S0022112080002595.

Gu, H., Stansby, P., Stallard, T., Carpintero Moreno, E., 2018. Drag, added mass and radiation damping of oscillating vertical cylindrical bodies in heave and surge in still water. J. Fluid Struct. 82, 343–356.

Hirt, C.W., Nichols, B.D., 1981. Volume of fluid (VOF) method for the dynamics of free boundaries. J. Comput. Phys. 39 (1), 201–225. https://doi.org/10.1016/0021-9991(81)90145-5.

Ishihara, T., Liu, Y., 2020. Dynamic response analysis of a semi-submersible floating wind turbine in combined wave and current conditions using advanced hydrodynamic models. Energies 13 (21), 5820. https://doi.org/10.3390/en13215820.

Ishihara, T., Zhang, S., 2019. Prediction of dynamic response of semi-submersible floating offshore wind turbine using augmented Morison's equation with frequency dependent hydrodynamic coefficients. Renew. Energy 131, 1186–1207. https://doi.org/10.1016/j.renene.2018.08.042.

Jensen, B.L., Sumer, B.M., Fredsøe, J., 1989. Turbulent oscillatory boundary layers at high Reynolds numbers. J. Fluid Mech. 206, 265–297. https://doi.org/10.1017/S0022112089002302.

Jonkman, J.M., 2007. Dynamics Modeling and Loads Analysis of an Offshore Floating Wind Turbine. https://doi.org/10.2172/921803.

Kikuchi, Y., Ishihara, T., 2020. Comparison of dynamic response and levelized cost of energy on three floater concepts of floating offshore wind turbine systems. In: Journal of Physics: Conference Series. Institute of Physics Publishing. https://doi.org/10.1088/1742-6596/1452/1/012035.

Kosasih, K.M.A., Niizato, H., Okubo, S., Mitani, S., Suzuki, H., 2019. Wave tank experiment and coupled simulation analysis of barge-type offshore wind turbine. In: Proceedings of the 29th International Ocean and Polar Engineering Conference, Honolulu, Hawaii, USA.

Molin, B., Lacaze, J., 2016. On approximations of the wave drift forces acting on semi-submersible platforms with heave plates. In: Proceedings of the ASME 2016 35th International Conference on Ocean, Offshore and Arctic Engineering, Volume 1: Offshore Technology; Offshore Geotechnics (Pp. V001T01A042). ASME, Busan, South Korea. https://doi.org/10.1115/OMAE2016-54166.

Molin, B., Remy, F., Rippol, T., 2007. Experimental study of the heave added mass and damping of solid and perforated disks close to the free surface. In: Proceedings of the 12th International Congress of the International Maritime Association of the Mediterranean (IMAM 2007), Varna, Bulgaria.

NEDO Demonstration Project of Next-Generation Offshore Floating Wind Turbine. https://www.nedo.go.jp/floating/. (Accessed 7 January 2023).

Newman, J.N., 1974. Second-order, slowly-varying forces on vessels in irregular waves. In: Proceedings of the International Symposium on Dynamics of Marine Vehicles and Structures in Waves. London, UK.

Otter, A., Murphy, J., Pakrashi, V., Robertson, A., Demond, C., 2021. A review of modelling techniques for floating offshore wind turbines. Wind Energy 25 (5), 831–857. https://doi.org/10.1002/we.2701.

Pan, J., Ishihara, T., 2019. Numerical prediction of hydrodynamic coefficients for a semi-sub floater by using large eddy method with volume of fluid method and Richardson extrapolation. In: Journal of Physics: Conference Series. Institute of Physics Publishing. https://doi.org/10.1088/1742-6596/1356/1/012034.

Pham, T.D., Shin, H., 2020. The effect of the second-order wave loads on drift motion of a semi-submersible floating offshore wind turbine. J. Mar. Sci. Eng. 8 (11), 1–13. https://doi.org/10.3390/jmse8110859.

Pinguet, R., Benoit, M., Molin, B., Rezende, F., 2022. CFD analysis of added mass, damping and induced flow of isolated and cylinder-mounted heave plates at various submergence depths using an overset mesh method. J. Fluid Struct. 109 https://doi.org/10.1016/j.jfluidstructs.2021.103442.

Robertson, A., Jonkman, J., Vorpahl, F., Popko, W., Qvist, J., Frøyd, L., Chen, X., Azcona, J., Uzunoglu, E., Soares, C.G., Luan, C., Yutong, H., Pengcheng, F., Yde, A., Larsen, T., Nichols, J., Buils, R., Lei, L., Nygard, T.A., Manolas, D., Heege, A., Ringdalen Vatne, S., Ormberg, H., Duarte, T., Godreau, C., Hansen, H.F., Nielsen, A.W., Riber, H., le Cunff, C., Abele, R., Beyer, F., Yamaguchi, A., Jung, K.J., Shin, H., Shi, W., Park, H., Alves, M., Guérinel, M., 2014. Offshore code comparison collaboration, continuation within IEA wind task 30: phase II results regarding a floating semisubmersible wind system. In: Proceedings of the ASME 2014 33rd International Conference on Ocean, Offshore and Arctic Engineering. Volume 9B. Ocean Renewable Energy. V09BT09A012. https://doi.org/10.1115/OMAE2014-24040.

Rusche, H., 2003. Computational Fluid Dynamics of Dispersed Two-phase Flows at High Phase Fractions. PhD Thesis. Imperial College of Science, Technology & Medicine.

Stansberg, C.T., Kaasen, K.E., Abrahamsen, B.C., Nestegård, A., Shao, Y., Larsen, K., 2015. Challenges in wave force modelling for mooring design in high seas. In: Offshore Technology Conference, Houston, Texas, USA. https://doi.org/10.4043/25944-MS.

Tan, L., Ikoma, T., Aida, Y., Masuda, K., 2021. Mean wave drift forces on a barge-type floating wind turbine platform with moonpools. J. Mar. Sci. Eng. 9 (7), 709. https://doi.org/10.3390/jmse9070709.

Weller, H.G., Tabor, G., Jasak, H., Fureby, C., 1998. A tensorial approach to computational continuum mechanics using object-oriented techniques. Comput. Phys. 12, 620. https://doi.org/10.1063/1.168744.

WindFloat 1. https://www.principlepower.com/projects/windfloat1. (Accessed 7 January 2023).

Zhang, S., Ishihara, T., 2020. Numerical study of distributed hydrodynamic force on a circular heave plate by large eddy simulations with volume of fluid method. Ships Offshore Struct. 15 (6), 574–586. https://doi.org/10.1080/17445302.2019.1661630.

Zhang, S., Ishihara, T., 2018. Numerical study of hydrodynamic coefficients of multiple heave plates by large eddy simulations with volume of fluid method. Ocean. Eng. 163, 583–598. https://doi.org/10.1016/j.oceaneng.2018.03.060.